Generalized approach for single-optical-access interferometric particle imaging

Christian Sax, Max Dreisbach, and Jochen Kriegseis*
Institute of Fluid Mechanics (ISTM), Karlsruhe Institute of Technology (KIT), Kaiserstr. 10, Karlsruhe 76131, Germany

(Received 29 March 2025; revised 21 July 2025; accepted 4 September 2025; published 27 October 2025)

Interferometric particle imaging (IPI) enables the sizing of small transparent particles, from a few microns to several millimeters, across a large field of view, which is not feasible with typical imaging-based methods. However, current IPI setups typically require two separate optical accesses—one for coupling the illuminating laser beam into the measurement volume, and another to allow the scattered light to exit toward the camera—thereby limiting their applicability in constrained environments. This work presents a generalized IPI approach suitable across all scattering regimes—including backscatter for single-optical-access configurations—and is applicable to both droplets and bubbles. This study demonstrates how the scattering angle influences signal-to-noise ratio (SNR), measurable size range, and uncertainty. Polarization significantly affects signal quality, particularly in backscatter. Variations in light intensity with angular variations can introduce position-dependent uncertainties, and the sensitivity of the size measurement (transfer function) varies with scattering angle. Experimental validation with bubbles confirms the feasibility of backscatter IPI despite lower SNR. For droplets, the reduction in SNR is less pronounced; however, the transfer function behaves differently compared to bubbles, making both evaluation and uncertainty estimation more complex. Additional effects like glare-point splitting can add redundancy but increase complexity. Overall, this study demonstrates that IPI in backscatter is not only feasible but also a key step toward single-sided optical access, expanding the method's practical applicability of the IPI method.

DOI: 10.1103/7kc3-7yyh

I. INTRODUCTION

Dispersed multiphase flows play a central role in numerous scientific and engineering problems. As such, their investigation is at the core of many research studies. Such flows are typically gas–liquid, gas–solid, or liquid–solid combinations in which a dispersed phase is surrounded by a continuous phase. In these types of flows, the continuous phase comprises the majority of the volume fraction. Typical examples include bubbly flow, sprays, and mist flow. In many applications, the particles of the dispersed phase become very small compared to the field of view, so that in-focus imaging techniques reach their resolution limit.

In the case of small particles, with diameters typically ranging from a few microns to a few millimeters, in a large field of view (spanning several millimeters to centimeters), interferometric particle imaging (IPI) has prevailed as one of the preferred techniques for quantification. IPI can be applied to any flow with a transparent continuous and dispersed phase, provided that the refractive indices of the two phases differ and the particles of the dispersed phase are approximately spherical. Although alternative techniques like optical coherence tomography (OCT) [1] and light detection and ranging (LIDAR) [2] offer useful capabilities for tomographic approaches, they are less suited to the goals of this study, since both are not immediate snapshot methods and rely on scanning or traversing to record the domain of interest. In contrast, IPI provides single-shot, full-field imaging as is crucial for resolving an instantaneous field of, for example, fast-moving particles in transient flows.

Examples of the use of IPI on droplet flows include the characterization of sprays [3,4], droplet analysis at nozzle outlets [5], droplets in combustion [6], and droplet analysis in clouds and the atmosphere [7–9]. Furthermore, investigations into bubbly flow have been conducted [10–12], with bubbly flow appearing in boiling and cavitation phenomena. Originally introduced as interferometric laser imaging for droplet sizing (ILIDS) and exclusively for droplets [13–15], the technique employs coherent, monochromatic light to illuminate the transparent particles of the dispersed phase. When observed from a scattering angle θ, interference patterns become visible at certain

*Contact author: jochen.kriegseis@kit.edu

Published by the American Physical Society under the terms of the Creative Commons Attribution 4.0 International license. Further distribution of this work must maintain attribution to the author(s) and the published article's title, journal citation, and DOI.

angles. The droplet size is then reconstructed from the interference pattern. The method was soon extended to bubbles [11,12] and renamed to the more general name interferometric particle imaging. Further developments include the consideration of higher-order frequencies in the interference patterns to create redundancy [16] and therefore increased precision, and the generalization of the IPI formula to arbitrary paraxial optical systems [17].

In the literature on IPI, the front-scatter region, with scattering angles of 66° for water droplets in air [13–15] and 45° for air bubbles in water [11,12], has been used predominantly due to its superior scattering efficiency and higher signal-to-noise ratio (SNR). More recently, scattering angles of 90°–110° have also been used [16,18,19]. However, there is still a lack of research on the use of IPI in the backscatter region. This is probably due to the lower SNR in the backscatter region, which makes the front-scatter region easier to deal with. In many cases, however, optical access is limited; for example, walls serve functional purposes and cannot be substituted by transparent materials (e.g., walls in fuel cells). This creates the need for backscatter-capable IPI, since measurements in the backscatter region reduce the number of required optical accesses to one.

In the scope of this work, a rigorous framework to conduct IPI in any scattering regime, including the backscatter regime, is presented. First, the theoretical basis and its extension to the backscatter region are explained. In the second part of this work, the main factors limiting the use of IPI, and influencing measurement limits and uncertainties, are elaborated.

II. THEORY OF INTERFEROMETRIC PARTICLE IMAGING

IPI utilizes the interference patterns of light scattered by approximately spherical particles to reconstruct their diameter d_p. The formation of the interference pattern and the reconstruction of the particle size are explained in this section. Two physical processes must be considered: light scattering at the particle, and interference of the scattered light.

A. Light scattering at the particle

First, only the scattering process at a bubble or droplet is regarded. Let us consider a single, transparent, approximately spherical particle with a refractive index n_1 that is different from the refractive index n_2 of the surrounds. The ratio between the refractive indices is then described by $m = n_1/n_2$ (i.e., relative refractive index). The scattering of light at the particle is initially described by the geometrical optics (GO) model. Light rays are either reflected or refracted at the particle surface (see Fig. 1). A light ray directly reflected at the particle surface is denoted as order zero, $p = 0$, while refracted light entering the particle is of order $p \geq 1$. The scattering order of the refracted light

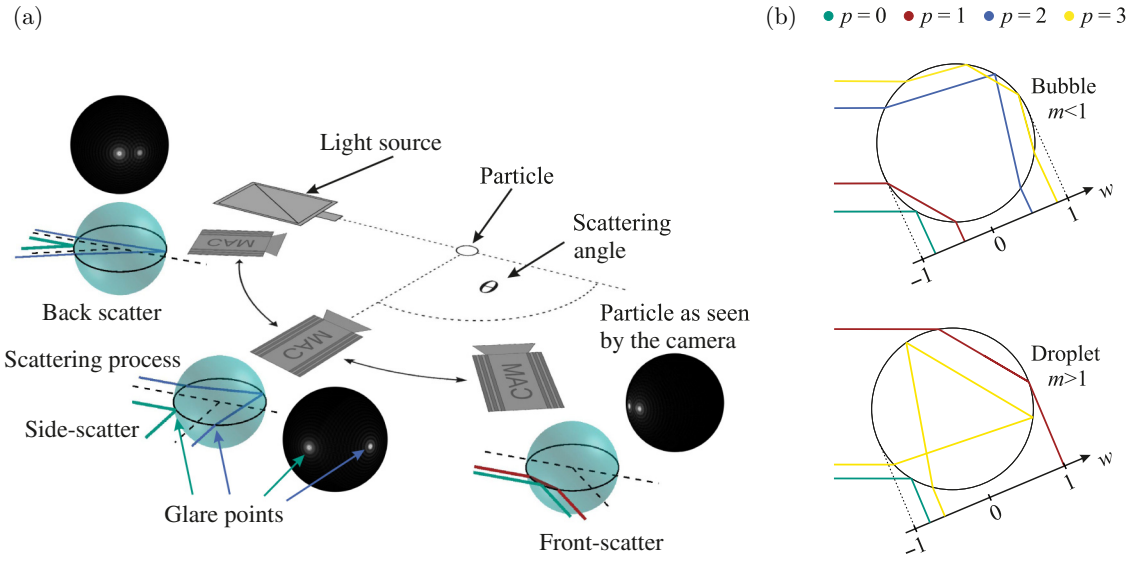

FIG. 1. Scattering on a sphere visualized by the GO model. (a) The relationship between the glare points and the scattering angle θ. The blue transparent spheres show the scattering of the dominant light rays at the corresponding scattering angle. The black spheres show the glare points as seen by the camera at that angle. (b) The relationship between the glare points and the refractive index. A bubble $m < 1$ (top) and a droplet $m > 1$ (bottom) are shown. Depicted are the reflected ray $p = 0$ (green), and the first three orders of refracted rays $p = 1$ (dark red), $p = 2$ (dark blue), and $p = 3$ (yellow). The position of the glare point on the sphere's surface is indicated by the w coordinate. Note that the light is monochromatic and the colors encode the scattering order.

describes the number of chords traveled inside the particle or $p-1$ internal reflections. The exit points of the light rays are called glare points and are perceived as bright spots on the particle surface when viewed from a scattering angle θ [20,21] [see Fig. 1(a)].

Only light rays that exit the particle in parallel with the angle θ eventually reach the camera, and thus all other rays can be discarded for this model. Furthermore, refraction at the particle surface is governed by Snell's law, which leads to two fundamental implications for the scattering process: the positions of the glare points depend on the scattering angle [see Fig. 1(a)] and on the relative refractive index [see Fig. 1(b)]. This mechanism causes, in particular, a disparity between particles with $m > 1$ (droplets) and $m < 1$ (bubbles). Furthermore, the intensity of the glare points also depends on the scattering angle, due to the angle-dependent transmission and reflection coefficients at the particle surface, as described by Fresnel's formulas. Therefore, different scattering angles are dominated by different scattering orders (usually not more than one or two orders at a time), as will be elaborated further in the remainder of the paper [see also Fig. 1(a)].

In a plane scattering process, glare points are located on the equator of the sphere. In analogy to the work of van de Hulst *et al.* [20,21], the position of a glare point on the particle surface is denoted by the normalized w coordinate, which represents the projection of the sphere's equator onto a straight line as seen by a camera [see Fig. 1(b)]. The position w_i of a glare point of order p_i can take values of $[-1, 1]$, with $|w| = 0$ representing the center and $|w| = 1$ the edges of the sphere as seen by the camera. With the GO model, w_i can be determined by geometrical considerations, as is illustrated in Fig. 2(a).

Based on the commonly used convention [11,13], the angle between the light ray and the tangent of the particle surface is defined as β. The angle of an incident ray of order p_i is denoted as $\beta_i^{(p_i)}$ and the angle of the transmitted ray is denoted as $\beta_t^{(p_i)}$. In the case of the reflected ($p = 0$) light ray, β_r is used for the incident ray. As the scattering angle θ is assumed to be known, Snell's law together with the sum of the angles provides two equations for the calculation of the two angles β_i and β_t. The glare-point position is then calculated from β_i and the particle diameter

$$w_i^{\text{phys}} = \frac{d_p}{2} w_i = \frac{d_p}{2} q \cos(\beta_i^{(p_i)}), \tag{1}$$

where w_i^{phys} is the distance in physical units (e.g., microns), w_i is the normalized position, and the factor $q = \pm 1$ indicates on which side of the sphere the glare point is located.

B. Formation of the interference pattern

While light is scattered in all directions, only the light traveling parallel to the optical axis reaches the camera and is therefore considered here. When the particle is illuminated with coherent, monochromatic light, the light scattered off the particle forms an interference pattern in the far field (distance from the particle $\gg d_p^2/\lambda$, with d_p being the particle size [23]). The underlying physical process is comparable to the one observed at a double slit in Young's fringe experiment [see Fig. 2(b)]. While the scattered light is visible as glare points when imaged in focus, the glare points become defocused rings when the observer is not located on the focal plane. At a sufficient distance from the focal plane, the defocus rings overlap to form an interference pattern [see Fig. 2(b) (bottom)].

The particle's diameter can then be reconstructed from the relationship between the number of stripes N_S in the interference pattern and the distance between the glare points. To relate the glare-point spacing to the number of stripes, either the distance between the particle and the observer or the opening angle of the aperture α_{AP} must be known. The relationship between the particle diameter and the number of stripes can be described for droplets ($m > 1$) [15,24] by

$$d_p = \frac{2\lambda N_S}{\alpha_{\text{AP}}} \left(\cos(\theta/2) + \frac{m \sin(\theta/2)}{\sqrt{m^2 - 2m\cos(\theta/2) + 1}} \right)^{-1} \tag{2}$$

and for bubbles ($m < 1$) [11,12] by

$$d_p = \frac{2\lambda N_S}{\alpha_{\text{AP}}} \left(\cos(\theta/2) - \frac{m \sin(\theta/2)}{\sqrt{m^2 - 2m\cos(\theta/2) + 1}} \right)^{-1}. \tag{3}$$

The problem with Eqs. (2) and (3) is that they are Taylor-series expansions [25] limited to the forward-scattering region (i.e., small θ) and to the scattering orders $p = 0$ and $p = 1$ that dominate this region. Equation (2) is restricted to $\theta < 2\arccos(1/m)$, which represents the total reflection of the $p = 1$ ray at the surface preventing the light from entering the sphere ($\beta_i^{(1)} \geq 0$). Equation (3) is limited to $\theta < 2\arccos(m)$ because the $p = 0$ and $p = 1$ glare points collapse into a single point. Consequently, Eqs. (2) and (3) cannot be used in the side- or backscatter regimes (i.e., large θ), since the angle relations do not hold true for this range and other scattering orders can dominate these regions.

Alternatively, only the relation between w_i^{phys} and the fringe frequency F of the interference pattern can be considered. This relationship is independent of the scattering angle and therefore avoids the first problem of Eqs. (2) and (3). This is done by introducing the glare-point (GP) distance between two glare points, $\Delta_{\text{GP}}^{\text{phys}} = |w_i^{\text{phys}} - w_j^{\text{phys}}|$ [see Eq. (1)]. With the formulas from Young's fringe experiment, the glare-point distance can be determined

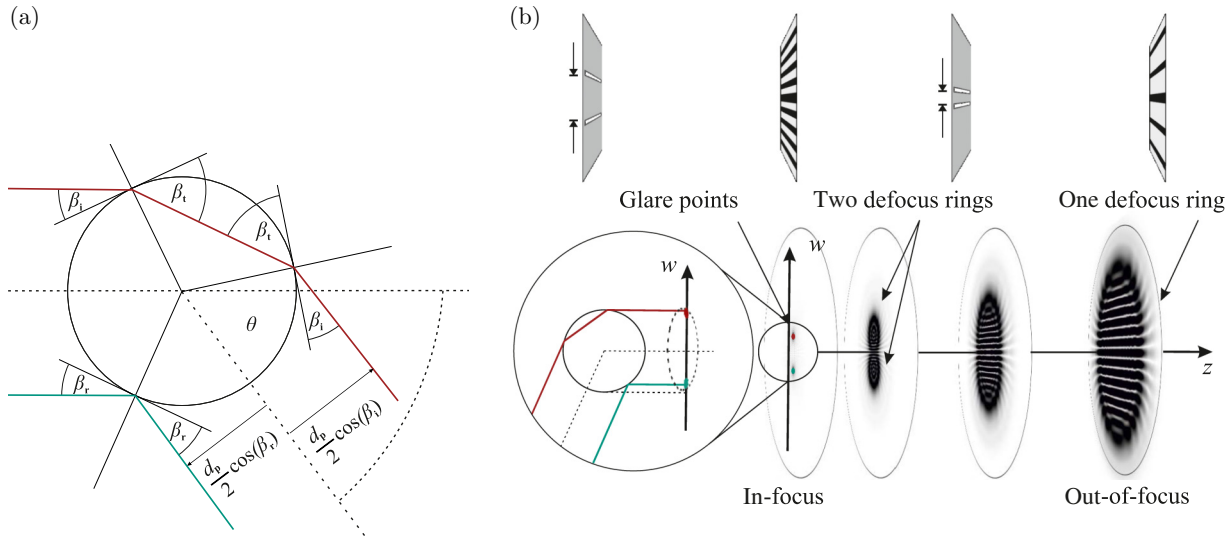

FIG. 2. (a) Light paths of the $p = 0$ and $p = 1$ rays through the particle using the GO model to determine the angular position of the glare point, on the example of a droplet. (b) The working principle of IPI is visualized. (bottom) From the observation angle θ, two glare points are visible on the particle surface, when imaged in focus. The images of the glare points begin to overlap and form an interference pattern as they move away from the focal plane. They eventually collapse into a single circle at a sufficient distance from the focal plane. (top) In addition, the analogy of the glare-point spacing (particle size) in IPI to a double slit in Young's fringe experiment [22] is visualized. The intensity maxima are depicted as dark stripes for better visibility (inverted intensity).

from [26]

$$\frac{1}{F} = \frac{\lambda_0 d_s / n_2}{\Delta_{\mathrm{GP}}^{\mathrm{phys}}}, \tag{4}$$

where d_s is the distance between the particle and the observer (i.e., the camera chip), and λ_0 is the wavelength of the light in vacuum. Equation (4) is constrained to the propagation of light waves in open space.

However, to change the direction of light and/or to separate different fluids, most measurement scenarios involve optical elements such as lenses and/or windows, and therefore a generalization to arbitrary paraxial systems is needed. Such systems can be comprehensively described by ray transfer matrices (also known as *ABCD* matrices) [27,28]. These matrices describe how the position and angle (with respect to the optical axis) of a ray change along two points on the optical axis. Such a matrix takes the form

$$M_{\mathrm{tot}} = \begin{bmatrix} A_{\mathrm{tot}} & B_{\mathrm{tot}} \\ C_{\mathrm{tot}} & D_{\mathrm{tot}} \end{bmatrix}, \tag{5}$$

where B_{tot} is the relevant entry for this work, as it describes the amount of defocusing. The parameter A_{tot} describes the magnification, C_{tot} is the negative inverse of the effective focal length, and D_{tot} describes the angular magnification of the system. The defocusing parameter B_{tot} replaces the expression d_s/n_2, for which it can be interpreted as the equivalent distance for propagation through free space representing the propagation through the optical system (with an imaging lens, etc.). More details on M_{tot} can be found in Appendix A.

Shen *et al.* [17] incorporated this approach into Eq. (4) to formulate

$$\frac{1}{F} = \left| \frac{\lambda B_{\mathrm{tot}}}{\Delta_{\mathrm{GP}}^{\mathrm{phys}}} \right|. \tag{6}$$

Whilst this equation solves the issue of the scattering-angle dependence, a formulation of the relationship between the glare-point distance and the particle diameter still needs to be found, in order to perform IPI. As described above, the glare-point position and visible glare-point orders do change with the scattering angle and the refractive index. For this reason, a general formulation is introduced as

$$\begin{aligned} \Delta_{\mathrm{GP}(\theta)}^{\mathrm{phys}(p_i,p_j)} &= |w_{p_i}^{\mathrm{phys}} - w_{p_j}^{\mathrm{phys}}| \\ &= \frac{d_p}{2}|w_{p_i} - w_{p_j}| = \frac{d_p}{2}\Delta_{\mathrm{GP}(\theta)}^{(p_i,p_j)}, \end{aligned} \tag{7}$$

which describes the glare-point separation as a function of the particle diameter and the position of any two glare points (p_i, p_j). The glare-point spacing introduces information from the scattering model into the interference model.

Equation (7) can be introduced into Eq. (6) to formulate a general relationship between the fringe frequency F and

the particle size d_p via

$$d_p = 2\left|\frac{\lambda B_{\text{tot}}}{\Delta_{\text{GP}(\theta)}^{(p_i,p_j)}}\right| F. \tag{8}$$

Unlike Eqs. (2) and (3), Eq. (8) can be applied to any scattering angle $\theta = [0, 180^\circ]$, but requires prior knowledge of the relative glare-point spacing $\Delta_{\text{GP}(\theta)}^{(p_i,p_j)}$. The GO model provides information on the position of the glare points but not on their intensity. The intensity I of the glare points plays a crucial role in determining which glare points form the interference pattern, since the intensity of individual glare points p_i might vary by several orders of magnitude with the scattering angle. Consequently, the interference pattern is not always the result of the same scattering orders, and some scattering angles do not give rise to visible interference patterns at all. A further model is, therefore, required to determine the glare-point spacing that produces the interference pattern.

III. THEORETICAL MODEL FOR IPI IN FRONT-, SIDE-, AND BACKSCATTER

This section presents a comprehensive method to choose a scattering angle in any scattering regime (front-, side-, and backscatter) for IPI. Two main questions are addressed: (i) Which scattering orders form visible interference patterns at which angles? (ii) What is the underlying spacing of the respective glare points that form the interference pattern?

A. Visibility of interference patterns

The intensity of the glare point of each scattering order depends on the scattering angle and the refractive index. As a result, interference patterns are not as clearly visible from all angles, if they are visible at all. Therefore, the first step is to identify scattering angles that produce visible interference patterns. In analogy to Young's fringe experiment, where the slits can be considered as point emitters of light, the glare points are modeled as point emitters [see Fig. 2(b)]. Thus it can be postulated that the scattering process at a particle leads to a visible interference pattern in the far field if the glare points act similarly to a double slit, as formulated in Theorem 1.

Theorem 1. A transparent, approximately spherical, particle with refractive index m, which is illuminated with monochromatic and coherent light, produces a visible interference pattern at a scattering angle θ if two glare points of order p_i and p_j have approximately the same light intensity $I_{(\theta)}^{(p_i)} \approx I_{(\theta)}^{(p_j)}$ (condition 1), and the two glare points p_i and p_j comprise the majority of the light intensity summed over all glare points $I_{(\theta)}^{(p_i)}, I_{(\theta)}^{(p_j)} \gg I_{(\theta)}^{(p_{k\neq i,j})}$ (condition 2).

Condition 1 ensures that the destructive interference of the two respective waves leads to intensity values close to zero and consequently results in good contrast between minima and maxima of the resulting fringe pattern. This condition has already been formulated in the literature [16,18]. However, condition 1 is necessary but not sufficient, so condition 2 takes into account all other glare points and ensures that the interference pattern is not eclipsed by light emitted by a third, even brighter, glare point (see Fig. 3). When measuring in the front-scatter region, no glare points other than $p = (0, 1)$ dominate and the sufficient condition is fulfilled automatically. For the side- and backscatter regimes, however, condition 2 is needed.

Theorem 1 provides the theoretical basis but needs to be formulated explicitly to be of practical use. Therefore, the intensity of the glare points needs to be quantified. A generally accepted model for the intensity of light scattered by particles in the size range relevant to IPI is the Lorenz-Mie theory (LMT) [20]. The LMT provides an exact solution to Maxwell's equations for the scattering of spherical waves at homogeneous spheres. The LMT uses the previously introduced relative refractive index m,

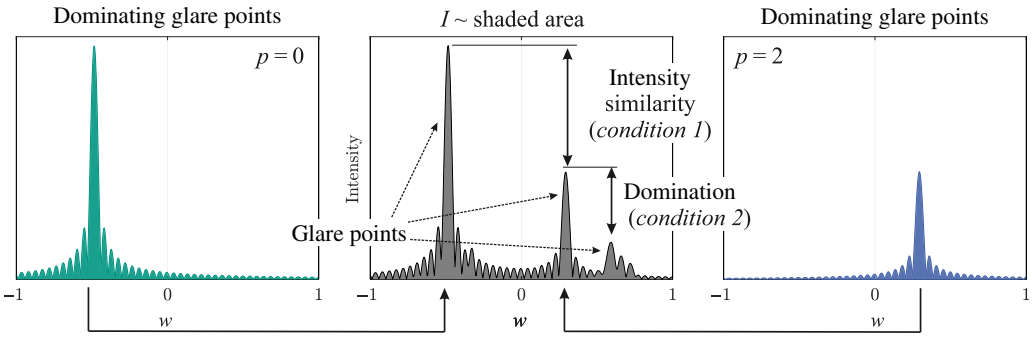

FIG. 3. The concept of visibility and the two conditions 1 and 2 are visualized in an example at a single scattering angle. Shown are the intensity over the projected particle surface as determined by the Lorenz-Mie theory (middle), and the decomposition into individual scattering orders with the Debye-series expansion (left and right). The glare points are the peaks of intensity.

where $\Re\{m\} = n_1/n_2$ and $\Im\{m\}$ describe the attenuation of the wave for partially opaque materials. In addition, a size factor $x = \pi d_p/(\lambda_0/n_2)$ is introduced for the dimensionless parametrization of the particle radius. Van de Hulst [20] derived the complex amplitude of the scattered light in the far field, $|S| = I$, from the LMT. The intensity is then calculated from the transverse electric (TE) S_1 and transverse magnetic (TM) S_2 modes of the wave via

$$I = \sqrt{S_{1(\theta)}^2 + S_{2(\theta)}^2}. \tag{9}$$

The LMT also considers the polarization of the light, which is a crucial feature for the contrast and intensity of interference patterns, as will be shown later. The complex amplitudes of the scattered light in the far field are given by [20]

$$S_{1(\theta)} = \sum_{k=1}^{\infty} \frac{2k+1}{k(k+1)} (a_k \Pi_{k(\theta)} + b_k \tau_{k(\theta)}), \tag{10}$$

$$S_{2(\theta)} = \sum_{k=1}^{\infty} \frac{2k+1}{k(k+1)} (b_k \Pi_{k(\theta)} + a_k \tau_{k(\theta)}), \tag{11}$$

where $\Pi_{k(\theta)}$ and $\tau_{k(\theta)}$ are the Mie angular functions, which represent a component of the spherical harmonics of order k that make up the electromagnetic wave. They represent the influence of the scattering angle. The Mie coefficients a_k and b_k, corresponding to TM waves (parallel polarization) and TE waves (perpendicular polarization), respectively, are functions of m and x, which weight the influence of each Mie angular function of order k on the wave. The Mie coefficients reflect the influence of the particle size and refractive index on the scattering process.

For particles relevant to IPI, the following assumptions can be made. The sphere is relatively large compared to the wavelength of light, $x \gg 1$; a large number of partial waves are considered, $k \gg 1$; and $\theta \neq \{0, 180\}$. Then $\Pi_{k(\theta)} \ll \tau_{k(\theta)}$ applies and therefore S_1 becomes associated with the TE mode and S_2 with the TM mode [20] (perpendicular and parallel polarization, respectively). The problem with the LMT, however, is that it provides only the integral intensity over all glare-point orders, whereas for IPI the intensity of individual glare points is of interest. Starting from the LMT, the integral intensity can be decomposed into individual scattering orders with the Debye-series expansion of the LMT [29]. The calculation of $S_{1(\theta)}$ and $S_{2(\theta)}$ by means of the Debye-series expansion is complex and computationally intensive. An efficient and straightforward calculation of $S_{1(\theta)}$ and $S_{2(\theta)}$ is possible by means of publicly available research software such as, e.g., MiePlot [30], which has been chosen in the present work (see Fig. 4).

Suitable scattering angles for IPI can be identified qualitatively from consideration of Fig. 4 in combination with Theorem 1, as shown in Figs. 4(a) and 4(b). For a quantitative evaluation of the visibility, however, an explicit formulation of Theorem 1 is needed. Condition 1 ensures that the two glare points forming the interference pattern have the same intensity, $I_{(\theta)}^{(p_i)}/I_{(\theta)}^{(p_j)} \approx 1$, and poses the necessary condition. Taking into account the phase difference between the two glare points, condition 1 can be quantified as follows [16,18]:

$$V_{\mathrm{C1}(\theta)}^{(p_i,p_j)} = \frac{2\sqrt{I_{(\theta)}^{(p_i)} I_{(\theta)}^{(p_j)}}}{I_{(\theta)}^{(p_i)} + I_{(\theta)}^{pj}} \approx 1. \tag{12}$$

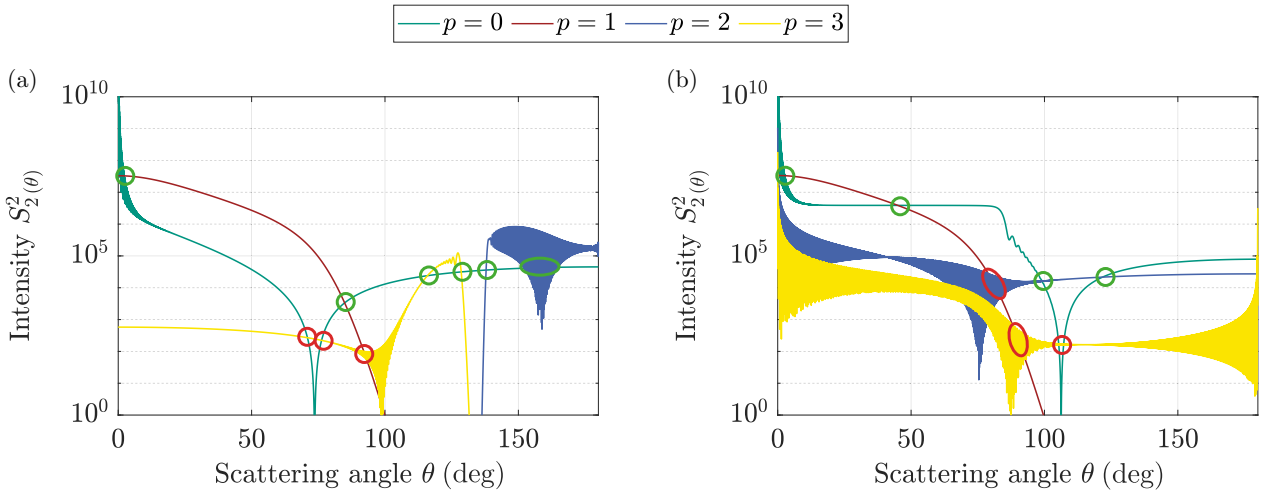

FIG. 4. The complex amplitude S_2^2 of each scattering order plotted over all scattering angles. Debye plots of the intensity of scattered light for (a) a water droplet in air ($m = 1.333 + i1.82\times10^{-9}$, $\lambda = 532$ µm, $d_p = 250$ µm $\Rightarrow$ $x = 1476.3$) and for (b) an air bubble in water ($m = 1/1.333 + i0$, $\lambda = 532$ µm, $d_p = 250$ µm $\Rightarrow$ $x = 1967.9$). The visibility criteria are visualized: scattering angles satisfying both criteria are ringed in green, whereas angles matching only the first condition but not the second one are ringed in red.

Condition 2 ensures that the glare points p_i and p_j that satisfy condition 1 are not eclipsed by other brighter glare points p_k, and thus states the sufficient criterion. In accordance with Eq. (12), Eq. (13) is formulated to approach unity when $I_{(\theta)}^{(p_i)}$ and $I_{(\theta)}^{(p_j)}$ comprise all the intensity of the scattered light. Therefore, the intensity of the considered glare-point pair is compared to the integral intensity over all scattering orders:

$$V_{\mathrm{C2}(\theta)}^{(p_i,p_j)} = \frac{2\sqrt{I_{(\theta)}^{(p_i)} I_{(\theta)}^{(p_j)}}}{\sum_{k=0}^{\infty} I_{(\theta)}^{(p_k)}} = \frac{2\sqrt{I_{(\theta)}^{(p_i)} I_{(\theta)}^{(p_j)}}}{I_{\mathrm{Mie}(\theta)}} \approx 1. \tag{13}$$

Since the Debye-series expansion approaches the Mie solution for the sum over all scattering orders $k \to \infty$, the simplification $\sum_{k=0}^{\infty} I_{(\theta)}^{(p_k)} = I_{\mathrm{Mie}(\theta)}$ can be used. This allows for the exact and faster computation of condition 2. Both Eqs. (12) and (13) are formulated in order to approach unity when the underlying condition is satisfied, with $V_{(\theta)} \in [0, 1]$.

Therefore, to give a quantitative description of Theorem 1, the two expressions can be multiplied to give

$$\begin{aligned} V_{(\theta)}^{(p_i,p_j)} &= V_{\mathrm{C1}(\theta)}^{(p_i,p_j)} V_{\mathrm{C2}(\theta)}^{(p_i,p_j)} \\ &= \frac{4 I_{(\theta)}^{(p_i)} I_{(\theta)}^{(p_j)}}{(I_{(\theta)}^{(p_i)} + I_{(\theta)}^{(p_j)}) I_{\mathrm{Mie}(\theta)}} \approx 1, \end{aligned} \tag{14}$$

while $V_{(\theta)} \in [0, 1]$ is preserved. The visibility of an interference pattern V_1 or V_2 for a TE or TM wave can be computed directly from the complex amplitudes S_1 or S_2 [Figs. 4(a) and 4(b)] to obtain Fig. 5. This allows the visibility to be quantified and the underlying scattering orders to be identified, solving the first problem mentioned in the introduction to this section. Equation (14) is valid for any transparent sphere with a homogeneous refractive index. As outlined above, two cases need to be distinguished for droplets ($m > 1$) and bubbles ($m < 1$). The most common examples in IPI are water droplets in air ($m = 1.333$) and air bubbles in water ($m = 1/1.333$), which will therefore be used as examples in this paper. For other refractive indices, the values presented in this work may change, but the outlined general effects remain the same for $m > 1$ or $m < 1$.

B. Visibility plots and examples

In this subsection, the visibility of interference patterns at different angles is discussed and the involved phenomena are elaborated. Figure 5 shows the visibility plot for water droplets in air and air bubbles in water with a diameter of $d_p = 250$ μm and light with $\lambda = 532$ nm. High values of $V_{1,2}$ correspond to better visibility. High visibility ultimately leads to better SNR (allowing for a better distinction between minima and maxima) and, consequently, to more reliable signal processing. However, the SNR also depends on the intensity of the scattered light itself, which is not considered in the visibility.

As expected, Fig. 5 predicts good visibility in the front-scatter regime at an angle of 66° for water droplets in TE mode and at 45° for bubbles in water in TE mode. It can also be seen that the orders $p = (0, 1)$ form an interference pattern, which is in agreement with the literature [11–15]. Figure 5 shows that these angles are preferable only in the TE mode, but in the TM-mode angles 84.5° for droplets and 41.6° for bubbles are preferable, while the $p = (0, 1)$ pair remains the dominant one. This demonstrates the importance of the polarization of the light used for IPI. However, for the scope of this work, the less explored side- and backscatter regions are of greater interest.

For water droplets and TE mode [see Fig. 5(a)], high visibility is achieved at scattering angles of 111°–129° with $p = (0, 3)$ and at 137.5°–165° with $p = (0, 2)$. The two regions are separated by an Alexander's dark band (ADB) [31], a region in which the intensities of the $p = 2$ and $p = 3$ glare points plummet. The ADB is encased by the rainbow angles, a phenomenon in which glare points of the same order collapse into a single glare point, increasing the intensity [21]. Both regions show a large variability of the visibility. This is undesirable because, as a particle moves through the field of view, the effective scattering angle varies slightly (up to a few degrees) and consequently interference patterns will be visible at some positions in the image but not at others. Water droplets in TM mode [see Fig. 5(b)] achieve similarly high visibility at scattering angles of 111°–129° with $p = (0, 3)$ and for angles larger than 137° with $p = (0, 2)$, again separated by an ADB. A major advantage of the TM mode is the lower variability of the visibility, especially in the range of 111°–129°, which renders TM a more reliable and robust choice.

For bubbles in TE mode [see Fig. 5(c)], the front-scatter region is the only region to yield a visibility of ≈ 100%. The $p = (0, 2)$ pair dominates most of the side- and backscatter regions but with lower visibility. The $p = (0, 3)$ pair reaches up to 86% visibility at 173°–179° but is again subject to strong fluctuations. Bubbles in TM mode achieve high visibility at 96°–101° and 114°–179° with $p = (0, 2)$ [see Fig. 5(d)]. The two regions are separated by the Brewster angle, a region where the $p = 0$ ray hits the surface at an angle at which the transmission coefficient is one and the reflection coefficient is zero. Consequently, no light is reflected at this point [see Fig. 4(b) at 106°]. Visibility drops sharply, as the intensity ratio at this point is very uneven. The two regions of high visibility show almost no fluctuations. Furthermore, the visibility in the range of 114°–179° is almost constant, making it ideal for use in IPI. Around 179.8°, the $p = (0, 3)$ pairing reaches up to 85% visibility but is subject to strong fluctuations.

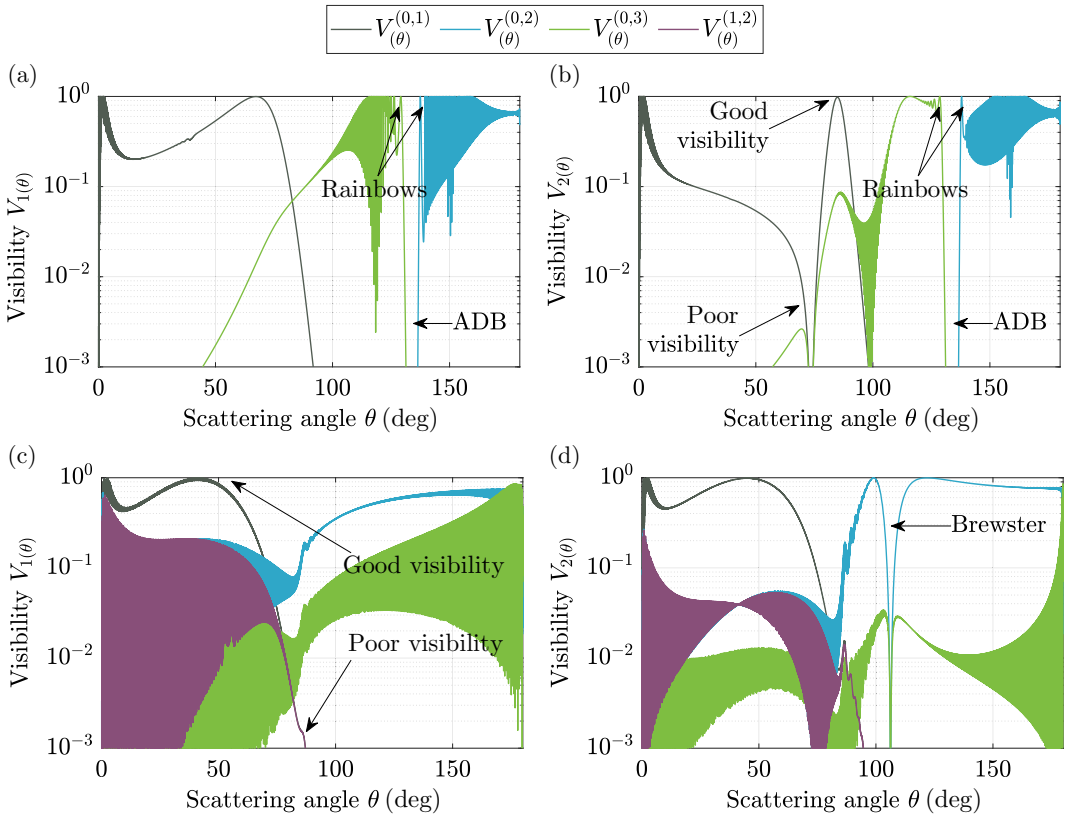

FIG. 5. Debye plots showing visibility over the scattering angle for (a,b) a water droplet in air ($m = 1.333 + i1.82\times10^{-9}$, $\lambda = 532$ µm, $d_p = 250$ µm $\Rightarrow$ $x = 1476.3$) in (a) TE mode (V_1) and (b) TM mode (V_2), and for (c,d) an air bubble in water ($m = 1/1.333 + i0$, $\lambda = 532$ µm, $d_p = 250$ µm $\Rightarrow$ $x = 1967.9$) in (c) TE mode (V_1) and (d) TM mode (V_2). A sufficient scattering angle for IPI is given whenever the visibility plot has a value close to 1. The glare-point pairings (0,1), (0,2), (0,3), and (1,2) are shown. In addition, the rainbow angles of the $p = 2$ and $p = 3$ scattering orders and Alexander's dark band (ADB) are marked in panels (a) and (b). The Brewster angle is marked in panel (d).

The above elaboration demonstrates that the TM mode is favorable for the side- and backscatter regimes, for both droplets and bubbles. This is remarkable information, since, for the forward scattering for droplets, usually the TE mode is used, while for bubbles both modes work in the forward-scattering region. Other effects such as ADB and the Brewster angles lead to regions of the scattering angle in which no interference pattern is visible and IPI cannot be performed. It is important to note that high visibility is necessary for IPI, but, for practical use, other effects such as SNR and uncertainties need to be taken into account too, which will be discussed in the following sections.

C. Determination of the glare-point spacing

The visibility plots contain information about appropriate scattering angles θ and the glare-point pairing (p_i, p_j) that forms the interference pattern. From this information, the value of the glare-point spacing $\Delta_{\mathrm{GP}(\theta)}^{(p_i,p_j)} = |w_{(\theta)}^{(p_i)} - w_{(\theta)}^{(p_j)}|$ can be determined as required for Eq. (8). This section presents two ways to compute the glare-point position $w_{(\theta)}^{(p_i)}$, which are interrelated but have different advantages. Additional effects not considered in the visibility considerations are discussed.

The first way to compute the glare-point positions is the derivation of the intensity over the particle surface from the complex amplitude S. Van de Hulst [21] introduced

$$A_{(w)} = \int_{\theta_0-\Delta\theta}^{\theta_0+\Delta\theta} S_{(\theta)} e^{-ixw(\theta_0-\theta)}\,\mathrm{d}\theta \tag{15}$$

as a way to obtain the intensity over the projected particle surface as indicated by w, here denoted as $A_{1(w)}$ and $A_{2(w)}$ corresponding to S_1 and S_2, respectively. This is done by applying a short-space Fourier transform on S over the angle range $\Delta\theta$ and around the desired scattering angle θ_0. Note that, while the positions w of the glare points do not change with the polarization, the intensities $A_{1(w)}$ and $A_{2(w)}$ of the glare points differ, as contrasted in Figs. 6 and 7 for droplets and bubbles, respectively.

Equation (15) effectively describes the propagation of the wave through a lens and shows how a camera would

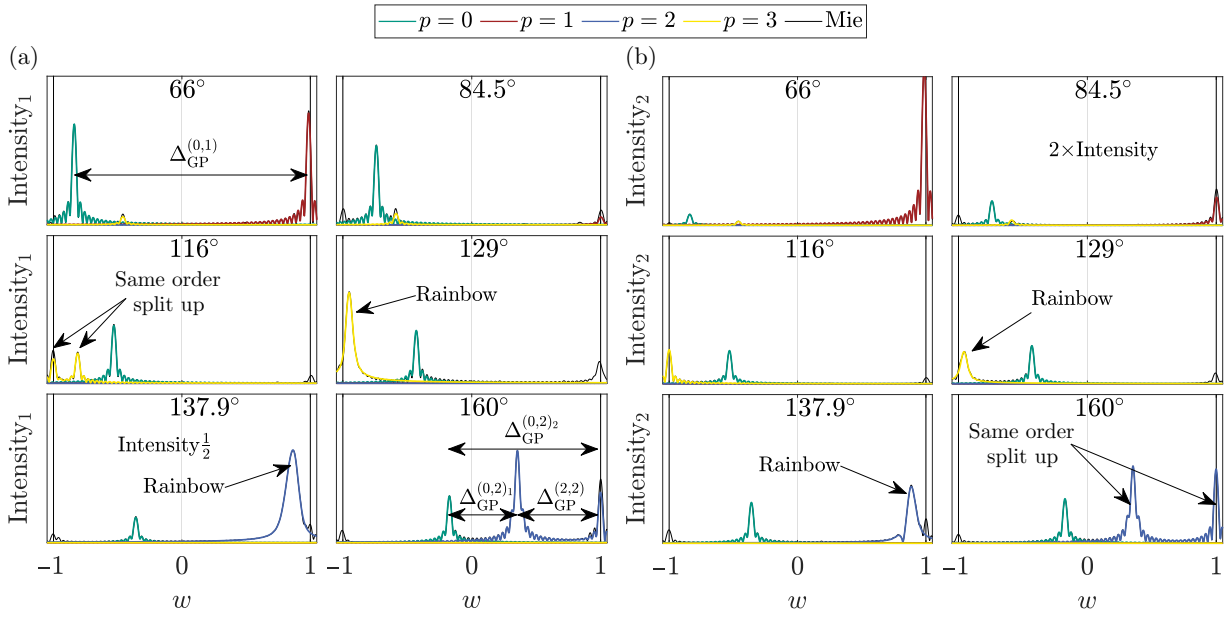

FIG. 6. Intensity over the particle surface (the glare points are the peaks). The scattering intensity $A_{(w)}$ is plotted over the particle surface w for a water droplet in air ($d_p = 250$ µm, $\lambda = 532$ nm $\Rightarrow$ $x = 1476.3$ and $m = 1.333 + i1.82\times10^{-9}$) in (a) perpendicular (TE) mode and (b) parallel (TM) mode. The scattering uncertainty $\Delta\theta = 3.7°$ was chosen based on the optical system used for the validation experiment. The scattering angle θ_0 around which $A_{(w)}$ was calculated is shown at the top of each plot. The intensities of the scattering orders $p = 0$ (green), $p = 1$ (dark red), $p = 2$ (dark blue), and $p = 3$ (yellow), as well as the integral intensity of all scattering orders (Mie intensity) (black) are shown. Unless otherwise indicated, all plots are on the same intensity scale.

see the glare points in focus. The angular range $\Delta\theta = \tan(\alpha_{AP})$ follows directly from geometrical considerations and is defined by the opening angle of the camera, α_{AP}, set by the aperture, which is the same angle as used in Eqs. (2) and (3). The opening angle is calculated from the triangle formed by the effective optical distance of the particle from the lens, $d_{p,\text{lens}}/n_2$, and the aperture diameter, d_{AP}, with $\tan(\alpha_{AP}) = d_{AP}n_2/(2d_{p,\text{lens}})$. While van de Hulst [21] introduced Eq. (15) for the integral intensity of all glare points (LMT), the complex amplitude $S_{(\theta)}^{(p_i)}$ from the Debye-series expansion of the LMT can be inserted instead of S_{Mie} to decompose the intensity into the individual scattering orders (see Fig. 3). The result is shown in Figs. 6 and 7 for droplets and bubbles, respectively, and hereafter referred to as glare-point plots. The glare-point position of scattering order p_i is then simply determined by finding the peak position of $A_{(w)}^{(p_i)}$. As Eq. (15) is a short-space Fourier transform, the uncertainty relation $\Delta\theta\,\Delta w = 1/x$ applies [21]. This means that for smaller particles the peaks become less distinct, to the point where the glare-point model collapses, i.e., when the particle approaches the size of the wavelength of light. For demonstration purposes, a large particle diameter has been arbitrarily chosen to make the discussed effects more salient.

The glare-point plots allow the intensity of the glare points to be assessed in a straightforward manner in addition to finding the glare-point spacing, as shown in Fig. 6(a). This allows one to judge the corresponding visibility intuitively. However, the disadvantage of this method is that each plot shows only a single scattering angle. Figure 6 shows a range of scattering angles with high visibility and other interesting effects. The first effect that can be seen is the influence of polarization on the intensity of the glare points, as can be identified from the comparison of Figs. 6(a) and 6(b) at $\theta = 66°$.

One effect that is not considered in the visibility considerations is that the same scattering order can produce more than one glare point, as discussed by van de Hulst [21] [see Fig. 6(b), $\theta = 160°$]. The intra-order split-up of glare points can cause a significant loss in intensity of the glare point as the light intensity is distributed over more than one glare point [see Fig. 6(a), $\theta = 116°$ and 129°]. This reveals a shortcoming of the visibility consideration, as it considers only the integral intensity of the scattering order at one scattering angle. If a single order splits into multiple glare points, then this integral intensity is also split between the two glare points of the same order, which cannot be captured by condition 1.

Such cases can nonetheless still be used for IPI and even have the advantage of introducing multiple frequencies due to the three glare-point spacings [see Fig. 6(a), $\theta = 160°$]. Dehaeck and van Beeck [16], for instance, used a third glare point of third order in side-scatter to create redundancy due to multiple frequencies being present in the interference pattern. This idea might also be extended to the use of intra-order split-ups to obtain

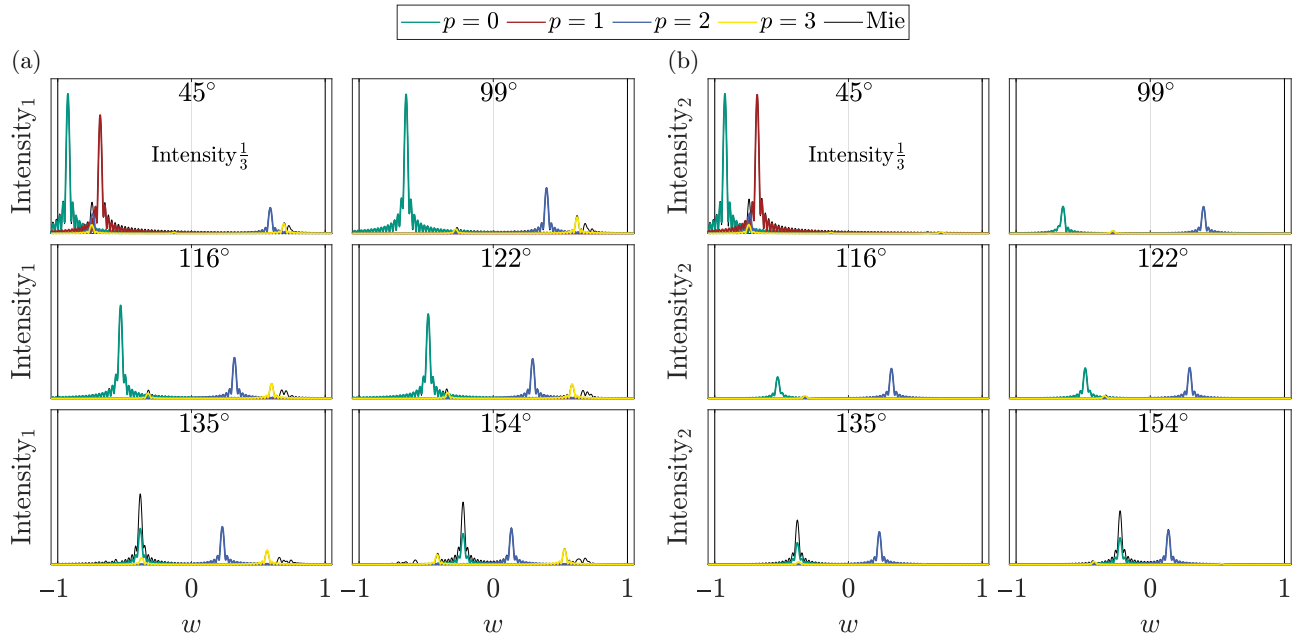

FIG. 7. Intensity over the particle surface (the glare points are the peaks). The scattering intensity ($A_{(w)}$) is plotted over the particle surface w for an air bubble in water ($d_p = 250$ µm, $\lambda = 532$ nm $\Rightarrow$ $x = 1967.9$ and $m = 1.333 + i1.82\times10^{-9}$) in (a) perpendicular (TE) mode and (b) parallel (TM) mode. The scattering uncertainty $\Delta\theta = 3.7°$ was chosen based on the optical system used for the validation experiment. The scattering angle θ_0 around which $A_{(w)}$ was calculated is shown at the top of each plot. The intensities of the scattering orders $p = 0$ (green), $p = 1$ (dark red), $p = 2$ (dark blue), and $p = 3$ (yellow), as well as the integral intensity of all scattering orders (Mie intensity) (black) are shown. Unless otherwise indicated, all plots are on the same intensity scale.

multiple frequencies from only two orders. Combined with the reasonably high intensity in backscatter for droplets, scattering angles around 160° can, therefore, be attractive for IPI. Note that the intra-order split-up for $p = 3$ at $\theta = 116°$ occurs only in the TE mode but not in the TM mode, again highlighting the importance of polarization for IPI. At certain angles, the so-called rainbow angles [21], two glare points of the same order collapse into a single glare point. The brightness of this rainbow glare point is substantially higher, since all light intensity of that order contributes to a single glare point [see Fig. 6(a), $\theta = 129°$ and 137.9°]. If two glare points of the same order are undesirable, measuring at the rainbow angles [21] can get around this problem. However, measurement at the rainbow angles is not preferable due to the uncertainty characteristics, as will be elaborated further in the following sections.

Bubbles show less complex phenomena (see Fig. 7). The TM polarization shows more uniform intensities between the glare points in side- and backscatter [see Fig. 7(b)]. However, the TE mode has the advantage of higher intensities [see Fig. 7(a), $\theta = 99°$–$154°$], which potentially compensates for the lower visibility (due to uneven intensity) with higher intensity-based SNR. For the TE mode, bubbles also show a third $p = 3$ glare point in the side- and backscatter regions [see Fig. 7(a), $\theta = 99°$–$154°$], and a third $p = 2$ glare point at 45°. Again, this third glare point could be used for multifrequency IPI as suggested by Dehaeck and van Beeck [16]. Unlike droplets, the side- and backscatter regimes have significantly lower intensities compared to the front-scatter regime, potentially resulting in lower SNR.

The second method to determine the glare-point spacing builds upon geometrical considerations, as shown in Fig. 1. This method uses Snell's law in combination with the reflection angles, which according to van de Hulst [21] leads to

$$\theta' = 2\left[\beta_i^{(p)} - p\arccos\left(\frac{1}{m}\cos(\beta_i^{(p)})\right)\right] = 2\pi k + q\theta \tag{16}$$

to calculate the angle of a ray relative to the surface tangent of the sphere. The two unknown constants $q = \pm1$ and $k \in \mathbb{N}$ are needed in order to formulate Eq. (16) without loss of generality for $m \lessgtr 1$ and arbitrary p. Solving this equation for $\beta_i^{(p)}$ then allows one to compute the glare-point position from $w^{(p)} = q\cos(\beta_i^{(p)})$. However, Eq. (16) is not easy to solve analytically and it is necessary to find values for q and k for which the equation has a real solution within $\beta_i^{(p)} \in [0, 90°]$. Therefore, an algorithm (Algorithm 1) for the indirect solution of Eq. (16) and the determination of the values of q and k is proposed and provided in

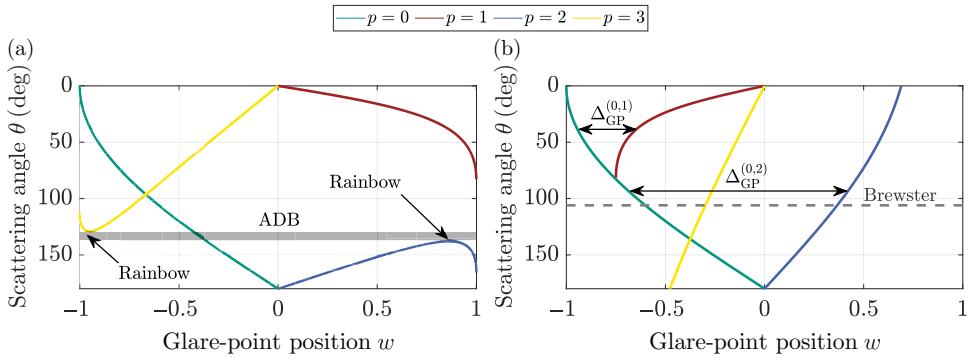

FIG. 8. Glare-point maps. Glare-point position w over the scattering angle visualized for the reflected and first three orders of refracted light rays for (a) a water droplet ($m = 1.333$) and (b) an air bubble in water ($m = 1/1.333$). For the droplet in panel (a), the rainbow angles and ADB are marked. For the bubble in panel (b), it is shown how to measure the glare-point spacing from the plots.

Appendix B. Furthermore, Table II lists values of q and k for $m \lessgtr 1$ and $p \in [0, 3]$ (see also Appendix B).

With the solution of Eq. (16), the glare-point position can be plotted over the scattering angle [see Figs. 8(a) and 8(b)], hereafter referred to as glare-point maps. The glare-point separation is determined by the horizontal distance between the two lines of the desired order [see Fig. 8(b)]. Unlike the first approach, no intensity information can be derived and therefore shortcomings of the visibility method cannot be identified with this approach. Accordingly, this also means that polarization effects cannot be assessed. However, the glare-point separation between a range of scattering angles can be easily compared using these glare-point maps. This allows one to investigate the change of glare-point spacing with the scattering angle. This is a crucial tool for deciding which scattering angle to choose, since the GP spacing has a major influence on the uncertainty and limitations of IPI (see following sections). Furthermore, the rainbow angles can be easily identified from this approach (with the condition $\mathrm{d}\theta/\mathrm{d}w = 0$, i.e., local minimum or maximum [21]).

The relationship between the two approaches can be understood as the three-dimensional interrelation of intensity, scattering angle, and glare-point position, which is accordingly visualized in Fig. 9. Both intensity and polarization, as well as the change in the glare-point spacing over scattering angles, are crucial quantities to consider for IPI. It is therefore advisable to consider both glare-point plots (Figs. 6 and 7) and glare-point maps (Fig. 8) when choosing a scattering angle to take all effects into account.

IV. EXPERIMENTAL VALIDATION OF BACKSCATTER IPI

In this section, the methodology derived above is validated experimentally. Equation (4) is the formulation for a double slit in Young's fringe experiment and has been well validated in physics. Also Eq. (6) introduced by Shen *et al.* [17] has been validated by, for example, Zhang *et al.* [18] by measuring the same bubble size distribution of air bubbles in oil at scattering angles of 45° and 90°. Equation (8) is a rearrangement of Eq. (6) with a model for the glare-point position added in $\Delta_{\mathrm{GP}}^{\mathrm{phys}}$.

To test the methodology outlined in this paper, a bubble generator with nominally constant bubble size distribution is chosen and characterized with IPI. Given the distribution function of the generated bubble sizes, its probability density function (PDF) can be considered constant and, consequently, the measured bubble size distributions should always be the same—regardless of the applied scattering angle. The test of the above working hypothesis is as follows: If IPI measurements based on the methodology outlined above all result in the same PDF, and interference patterns are visible at the predicted scattering angles, then the suggested method is valid. Based on Fig. 5(c), six different scattering angles were chosen, i.e., 45°, 99°, 116°, 122°, 135°, and 154° inside the water at the bubble. To validate Eq. (6) [17], the results at an angle of 45° are additionally compared with Eq. (3) [11,12].

A. Experimental procedure

In order to conduct the outlined test verification approach, an experimental setup as shown in Fig. 10

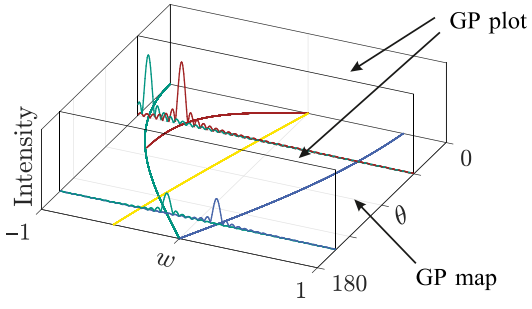

FIG. 9. Interrelationship between intensity, scattering angle θ, and glare-point position w. Glare-point plots represent vertical slices placed on the glare-point maps (horizontal slice).

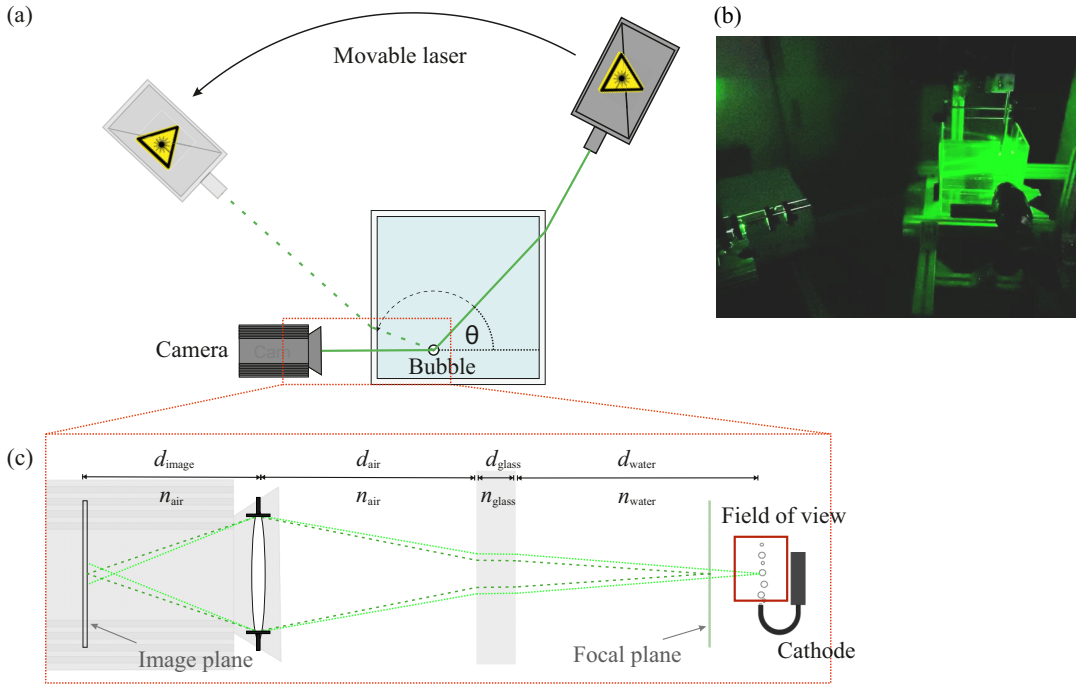

FIG. 10. The optical system of the validation experiment. Depicted are (a) the schematic principle of the experimental setup, and (b) an image of the real experimental setup. (c) A schematic close-up of the physical model for the optical path from the bubble generator (cathode) to the camera, showing the field of view relative to the tip of the cathode hook.

was constructed that was able to generate a constant distribution of bubbles. The setup allowed the scattering angle to be varied without changing the optical path since even small changes in the optical path can affect the result [see Fig. 10(a)].

To achieve a bubble generation with a constant size distribution, a generator based on electrolysis was constructed. The bubble generator consisted of two stainless-steel rods sheathed in black rubber for electrical insulation except at the ends. Both steel rods were connected to a power source, which provided a constant current and voltage throughout the measurements. A sheathed silver wire was connected to the end of the cathode (via a borehole). The wire was bent into a hook shape and only the last 0.5 mm of the wire was left unsheathed [see Fig. 10(c), right]. In this way, bubbles were generated only at the tip of the hook (known location). The field of view was placed directly on the top of the hook to ensure that the measured bubbles were at a known distance from the camera chip. The medium surrounding the bubbles was distilled water, with NaCl added to ensure conductivity. The generated hydrogen bubbles had a relative refractive index of $m = 1/1.333$. The point of bubble generation was placed in a water tank (glass $n = 1.52$, $20 \times 20 \times 20$ cm^3, 4-mm wall thickness) and fixed at a submersion depth of 4.1 cm.

A camera (PCO Pixelfly, CCD chip, 14-bit, 1392×1040 px^2, pixel size 6.45×6.45 μm^2; equipped with a Nikon Micro-Nikkor imaging lens, effective focal length 105 mm, aperture number f /4) was positioned on an arm outside of the tank at a fixed distance from the glass. A laser (Quantel Evergreen Nd:YAG, $\lambda = 532$ nm, 200 mJ/pulse) was positioned on a rotating arm to allow for different scattering angles without a change in the optical path from the bubble to the camera [see Fig. 10(b)]. Note that the laser head was oriented such that measurements took advantage of the favorable TE mode with correspondingly higher intensity of the scattered light (at the expense of lower visibility); see Fig. 7.

The laser and camera were synchronized in a single-pulse, single-exposure setup. The optical system is shown in Fig. 10(c). The distance from the bubble to the inner glass wall was $d_{water} = 125.5$ mm and the thickness of the glass wall was $d_{glass} = 4$ mm ($n_{glass} = 1.52$). The principal plane was located at the defocused position of $d_{air}^{defoc} = 11.71$ mm, and the image distance from the principal plane to the camera chip was $d_{image} = 21.81$ mm. Since a multilens camera lens was used, the position of the principal plane was unknown, so d_{image} and d_{air} were calculated from imaging a calibration target at the position of the bubble generator. The thin-lens equation

$$1/d_{obj}^{eff} + 1/d_{image}^{eff} - 1/f_{lens} = 0 \tag{17}$$

with $d_i^{eff} = d_i/n_i$ for the effective distances in combination with the magnification condition provide two equations to calculate d_{image} and d_{air}^{foc}. When moving the camera out

of focus by Δd_{air}, the value $d_{\text{air}}^{\text{defoc}} = d_{\text{air}}^{\text{foc}} + \Delta d_{\text{air}}$ can be calculated (see Appendix A for more details). The resulting defocusing parameter from the ray transfer matrix, describing the optical system, was $B_{\text{tot}} = -7.57$ mm [see Eq. (A4)].

B. Data processing

A total of 1200 images was recorded per angle and the laser brightness was adjusted at each angle to obtain sufficient intensity. Example results are shown in Fig. 11 for all investigated scattering angles. The images were preprocessed using mean image subtraction to subtract the background with only little loss of SNR. Morphological closing (dilation and erosion) was applied to the mean-subtracted images followed by a Hough transform to identify the circular particle images (PIs). The detections from the Hough transform were transferred into a bounding box around the particle (kernel). This was done for all angles except 154° since the Hough transform had a large detection miss rate due to the lower SNR and the bounding boxes had to be drawn manually. The underlying problem for this seeming shortcoming is that the light scattered by larger particles is brighter and therefore larger particles have higher SNRs. As the smaller particles accordingly have lower SNRs, the detection algorithm is unable to detect them and a sampling bias toward larger particles is introduced, thus falsifying the estimated PDF. This limitation necessitated manual labeling of the 154° images to avoid the sampling bias. At the other angles, the PIs were sufficiently distinct from the background for the detection algorithm to operate without bias.

The validation experiment shows that interference patterns are visible for all angles predicted with Fig. 5(d), as can be seen in Fig. 11(a). This shows that the visibility criterion formulated in Eq. (14) can be used for real experiments to identify applicable scattering angles for IPI. Furthermore, Fig. 7(a) predicts a third glare point at 45° for the TE mode. The effect of a third glare point can also be observed in the experiments [see Fig. 11(a), 45°], as the maxima from the primary glare-point pairing also have stripes from a secondary frequency, which is the effect of a third glare point.

A Laplacian filter was applied to the kernel to enhance the edges while preserving their position. The kernel was then averaged along the stripes to increase the SNR. The signal was low-pass-filtered using an FFT with a frequency cutoff to further reduce noise. The fringe frequency was then determined in two steps. First, a peak-finding algorithm was applied to the filtered signal to determine a frequency prior to the peak-to-peak distance. This step was necessary so that the subsequent fitting algorithm did not fit the envelope frequency (the rectangle function resulting from the defocused circle). Then, a first-order Fourier function was fitted on the raw signal [average along the stripes, see also Fig. 12(a), alongside the uncertainty discussion in Sec. V A], starting from the frequency prior.

To check the measured distributions for statistical significance, the statistical measure $\sum_{i=3}^{N} \sigma_{(d_1,\ldots,d_N)}/\mu_{(d_1,\ldots,d_N)}$ (standard deviation normalized by mean) was examined starting from $i = 3$ sampled bubbles (three, as the minimum for the standard deviation) and gradually increasing the considered sample size up the number of

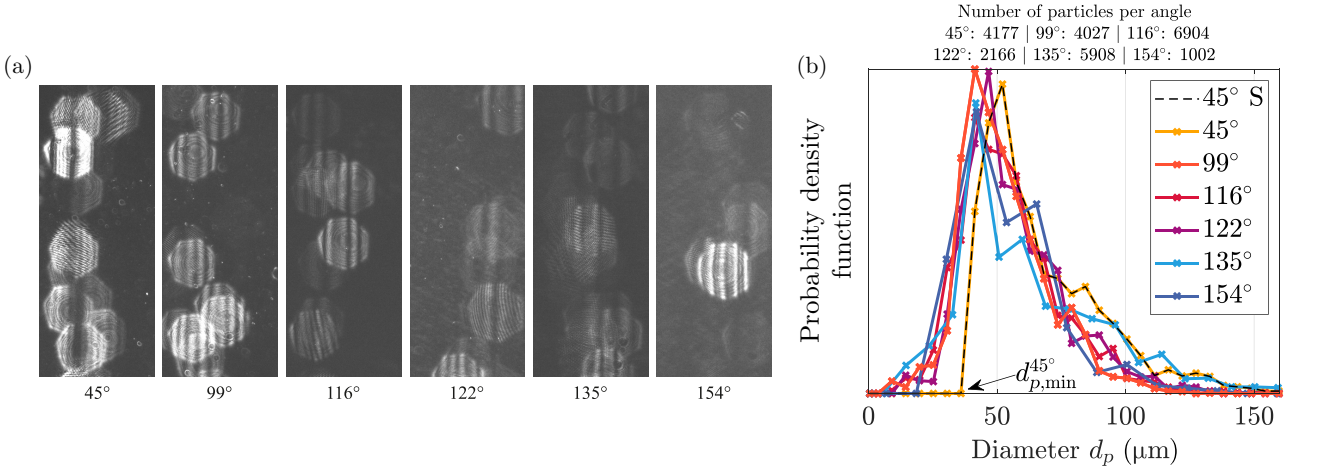

FIG. 11. Experimental results of the validation experiment. (a) Raw images from the validation experiment. For the image at 45°, a secondary frequency can be observed, which is the result of a third glare point ($p = 2$) in the TE mode. It can be seen that the particles visually become less distinct from the background and the intensity decreases in the backscatter region. (b) The determined PDFs of bubble radius for all investigated scattering angles 45°, 99°, 116°, 122°, 135°, and 154° (angle in water at the bubble). The numbers of particles in each PDF are shown above the graph. For the scattering angle of 45°, the PDF was evaluated with both Eq. (3) (45° S) and Eq. (8) (45°). The smallest measurable bubble diameter for $\theta = 45°$ was reached and is marked with $d_{\text{min}}^{45°}$. The PI brightness in the raw images in panel (a) is lower at higher scattering angles, as the overall intensity of the interference pattern is reduced. This can be observed by comparing with the intensity in Fig. 13.

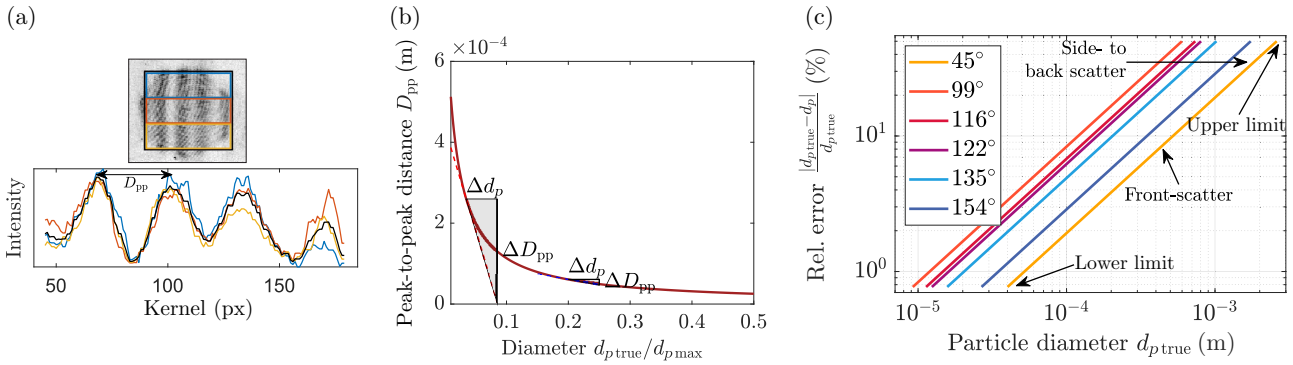

FIG. 12. (a) The different kernels used to average the signal along the maxima of the interference patterns and the resulting signal across the PI. At the top, the intensity is shown inverted for better visibility. (b) The peak-to-peak distance between the maxima of the interference pattern over the radius ($\theta = 45°$). (c) The uncertainty over bubble radius, i.e., the relative error (for an uncertainty of 1 px) in the measurement of the peak-to-peak distance over the particle diameter for different scattering angles (for the setup used in the validation experiment). In addition, the upper and lower limits of the measurable particle diameters at each scattering angle can be determined from the respective ends of the error lines.

measured bubbles N. Statistical convergence was observed around $N_{\text{bubbles}} \approx 800$ bubbles. The measurements include at least twice as many particles, except for the 154° evaluation, which was limited to 1000 particles due to manual labeling.

Figure 11(b) shows that the measured PDFs of the bubble diameter collapse, and according to the testing hypothesis this consequently means that the method works for IPI in any scattering regime. The same size distribution was measured at each scattering angle, which demonstrates that the shift in glare-point spacing $\Delta^{(p_i,p_j)}_{\text{GP}(\theta)}$ for Eq. (8) was correctly compensated when using Figs. 7 and 8. Small variations in the PDFs were within the measurement uncertainty, which is quantified in the next section. A closer look at Fig. 11(a) shows that, although interference patterns are clearly visible, PIs in the backscatter region are significantly less distinct from the background than PIs in the front-scatter region. This shows that, although the visibility provides the theoretical basis for finding interference patterns, other aspects such as the SNR need to be considered additionally in real experiments. The reduced signal quality in the backscatter regime and the different values of $\Delta^{(p_i,p_j)}_{\text{GP}(\theta)}$ affect the uncertainties and boundaries of the experiment, as will be elaborated further in Sec. V.

V. UNCERTAINTIES AND LIMITATIONS OF IPI

This section provides an overview of the main sources of uncertainty in the first subsection and a further discussion of the influencing factors in the second subsection.

A. Sources of uncertainty

In the calculation of the particle diameter by means of Eq. (8), three terms in the equation are subject to uncertainty: B_{tot}, which describes the distance from the focal plane; the glare-point spacing, $\Delta^{(p_i,p_j)}_{\text{GP}(\theta)}$; and the fringe frequency, F (assuming λ is well known, which holds true for typical lasers).

For the present case the out-of-focus location of the bubbles was quasi-constant, and accordingly considered known and fixed. This means that B_{tot} can be obtained from the calibration of the measurement. The camera was moved on a precision traverse to focus on a calibration target so as to obtain the unknowns d_{image} and d_{air} as described in Sec. IV. The precision of this calibration step is limited by the depth of field of the mounted lens, which was experimentally determined to be less than 10 μm. This uncertainty can be incorporated into the thin-lens equation and the magnification condition to investigate the effect on the calculation of d_{image} and d_{air}, and the subsequent effect on B_{tot}. For the given depth of field and optical system, the resulting uncertainty of $\Delta B_{\text{tot}} = 0.005\%$ can be considered negligible. Note, however, that, in a scenario where the distance from the particle to the camera is not fixed, B_{tot} becomes a function of the distance, and its uncertainty is likely to be significantly larger. That is, the corresponding estimation depends on the methods used to obtain the distance of the particle to the camera, which, however, is beyond the scope of the present work.

The uncertainty $\Delta^{(p_i,p_j)}_{\text{GP}(\theta)}$ in the second term in Eq. (8) stems from the uncertainty in the scattering angle. This uncertainty can arise either from the measurement setup (positioning of laser and camera) or from the motion of the particles perpendicular to the stripes of their interference pattern (here left and right in the image, $\theta = \theta_0 \pm \Delta\theta$). In both cases, this is a deterministic error. As shown in Fig. 8, even such small changes in θ can change the glare-point spacing. This relationship is highly nonlinear and depends on the scattering angle. A further discussion and quantification of this uncertainty is given in Sec. V B. For

TABLE I. Uncertainty as a systematic error introduced by an angle uncertainty of 1°.

θ (deg)		45	99	116	122	135	154
$\left\lvert\frac{\Delta_{GP}^{Err}-\Delta_{GP}}{\Delta_{GP}}\right\rvert$	(%)	3.40	1.07	1.42	1.63	2.17	3.78

the present validation experiment, a conservative upper limit for $\Delta\theta$ of 1° was chosen. The resulting new glare-point spacing Δ_{GP}^{Err} can be read directly from Fig. 8. For the scattering angles used, the resulting uncertainties are given in Table I. A different glare-point spacing changes the frequency of the interference pattern, thus mimicking a change in particle diameter and corresponding changes in the interference pattern (both change the glare-point spacing). This, in turn, also explains the variation of observed fringe frequencies for similar particles at different scattering angles.

The last term to consider is the fringe frequency, which is subject to measurement uncertainty and occurring stochastic error. The frequency measurement is affected by a variety of factors such as SNR, optical aberrations, and the performance of the algorithm used to extract the frequency, all of which render a theoretical quantification difficult. Therefore, an experimental approach was used to estimate an upper bound for the uncertainty. The algorithm to extract the fringe frequency was applied four times to the same interference pattern, each time using a different kernel [see Fig. 12(a), upper part]. Each kernel was averaged along the stripes to obtain a signal, which would result in slightly different frequencies [see Fig. 12(a), lower part]. The absolute spread of the frequencies determined would then give an estimate of the frequency uncertainty. For further investigation, the peak-to-peak distance in the fringe signal $D_{pp} = 1/F$ is used as the complement metric of F for more intuitive handling. This measure describes the distance between two maxima in the interference pattern [see Fig. 12(a), lower part]. The algorithm used showed a spread between 0.1 and 0.9 px in D_{pp} for the same particle and is, therefore, subpixel accurate in the frequency determination. However, a conservative upper limit of $\Delta D_{pp} = 1$ px was chosen for further investigation.

This metric then allows one to quantify some fundamental properties of the frequency measurement. The lowest frequency that can be measured (i.e., the smallest particle) corresponds to just one wavelength present in the PI, i.e., $D_{pp} = d_{PI}$, where d_{PI} is the PI diameter. The upper limit is given by the Nyquist criterion, for which the distance between peaks is $D_{pp} = 2$ px, which is the minimum distance between two maxima to be distinguishable without aliasing effects (giving the largest measurable particle). The relationship between particle diameter and peak-to-peak distance is nonlinear, $D_{pp} \sim 1/d_p$ (since $F \sim d_p$) [see Fig. 12(b)]. For small particles the frequency is highly resolved (here 130 px per signal wavelength), whereas for larger particles the frequency is less well resolved. This is directly related to the measurement uncertainty of the diameter. As shown in Fig. 12(b), Δd_p depends on the gradient $|\mathrm{d}D_{pp}/\mathrm{d}d_p|$ and is approximated as

$$\frac{\mathrm{d}D_{pp}}{\mathrm{d}d_p} = \frac{\Delta D_{pp}}{\Delta d_p}. \tag{18}$$

Equation (18) can be inserted into Eq. (6) to obtain

$$\Delta d_{p(d_p,\theta)} \leq \left\lvert\frac{\lambda B_{tot}\Delta D_{pp}}{\Delta_{GP(\theta)}}\right\rvert d_p^2, \tag{19}$$

which depends on the particle diameter and the scattering angle due to the glare-point spacing. This relation can be used to investigate the relative error over the particle diameter, for different scattering angles [see Fig. 12(c)].

Note that Eq. (19) gives an estimate for the upper limit, but does not quantify the uncertainty exactly. It can be seen from Fig. 12(c) that the scattering angle changes the uncertainty of the frequency determination for a constant particle size. This means that the upper and lower limits of measurable particle sizes are also dependent on the scattering angle. The corresponding uncertainty is, therefore, shifted in the same way. For bubbles, the largest diameter may be measured in front-scatter, while the smallest bubbles may be measured in side-scatter, with the backscatter regime approaching the uncertainty of the front-scatter regime. This is a crucial insight, as an experimentalist might then choose a scattering angle based on the expected particle size distribution. This also shows that a scattering angle should be chosen to measure close to the lower limit, as the uncertainties are significantly lower. The frequency uncertainty approaches 50% at the Nyquist diameter and is therefore the dominant uncertainty for large particles.

B. Main influences on the uncertainty

The previous subsection discussed the quantities that are subject to uncertainty; this subsection focuses on the main sources of these uncertainties. While Fig. 12(c) would suggest very similar properties between the front- and backscatter regimes for bubbles, this is not the case, due to the significantly lower SNR in backscatter. The SNR is a result of the PI intensity compared to the background noise on the camera chip. The performance of the algorithm to measure ΔD_{pp} is dependent on the SNR. While this relationship depends on the algorithm, it can be generally assumed that better performance (i.e., lower ΔD_{pp}) is obtained with higher SNR. The SNR depends on several factors, mainly the particle diameter, the scattering angle, and the amount of defocusing z_{defoc}. Consequently,

Eq. (19) must be modified to

$$\Delta d_{p(d_p,\theta,z_{\text{defoc}})} \leq \left| \frac{\lambda B_{\text{tot}(z_{\text{defoc}})} \Delta D_{\text{pp},(\text{SNR}(\theta,z_{\text{defoc}},d_p))}}{\Delta_{\text{GP}(\theta)}} \right| d_p^2, \tag{20}$$

which accounts for the fact that ΔD_{pp} is not constant. One important factor is the particle size, since larger particles result in brighter interference patterns, as can be proven by the LMT [20]. This suggests that ΔD_{pp} becomes smaller with larger particles, counteracting $\Delta d_p \sim d_p^2$. Furthermore, this means that Eq. (19) overestimates the uncertainty for large particles and underestimates it for smaller ones. This is advantageous, as it indicates that large particles can be measured with smaller uncertainties than Eq. (19) suggests.

The relationship between intensity and particle diameter is exponential, suggesting radically better SNR for large particles. A second influence on the SNR is the distance of the particle from the focal plane z_{defoc}, which is also taken into account in B_{tot}. The intensity of the PI decreases with the distance from the focal plane, resulting in a lower SNR. As the diameter of the PI increases approximately linearly with the distance from the focal plane [32], the area of the PI increases by the power of 2. As the light intensity is distributed over a larger PI area, the intensity of the PI becomes accordingly weaker and the SNR decreases. At the same time, however, a more defocused particle results in larger PIs [17,32], as indicated in Fig. 2(b), which in turn results in better interference pattern resolution and lower ΔD_{pp}. Consequently, there are two counteracting effects on ΔD_{pp} when z_{defoc} is changed: The increase in the resolution of the interference pattern is countered by the decrease in the SNR of the pattern. The increase in fringe frequency resolution is linear with sufficient distance from the focal plane [33], while the intensity loss decreases with the power of 2. The linear increase of resolution coupled with the quadratic decrease of SNR indicates that there is an optimal amount of defocusing for the PI, which is in agreement with earlier PI-characterization studies [34].

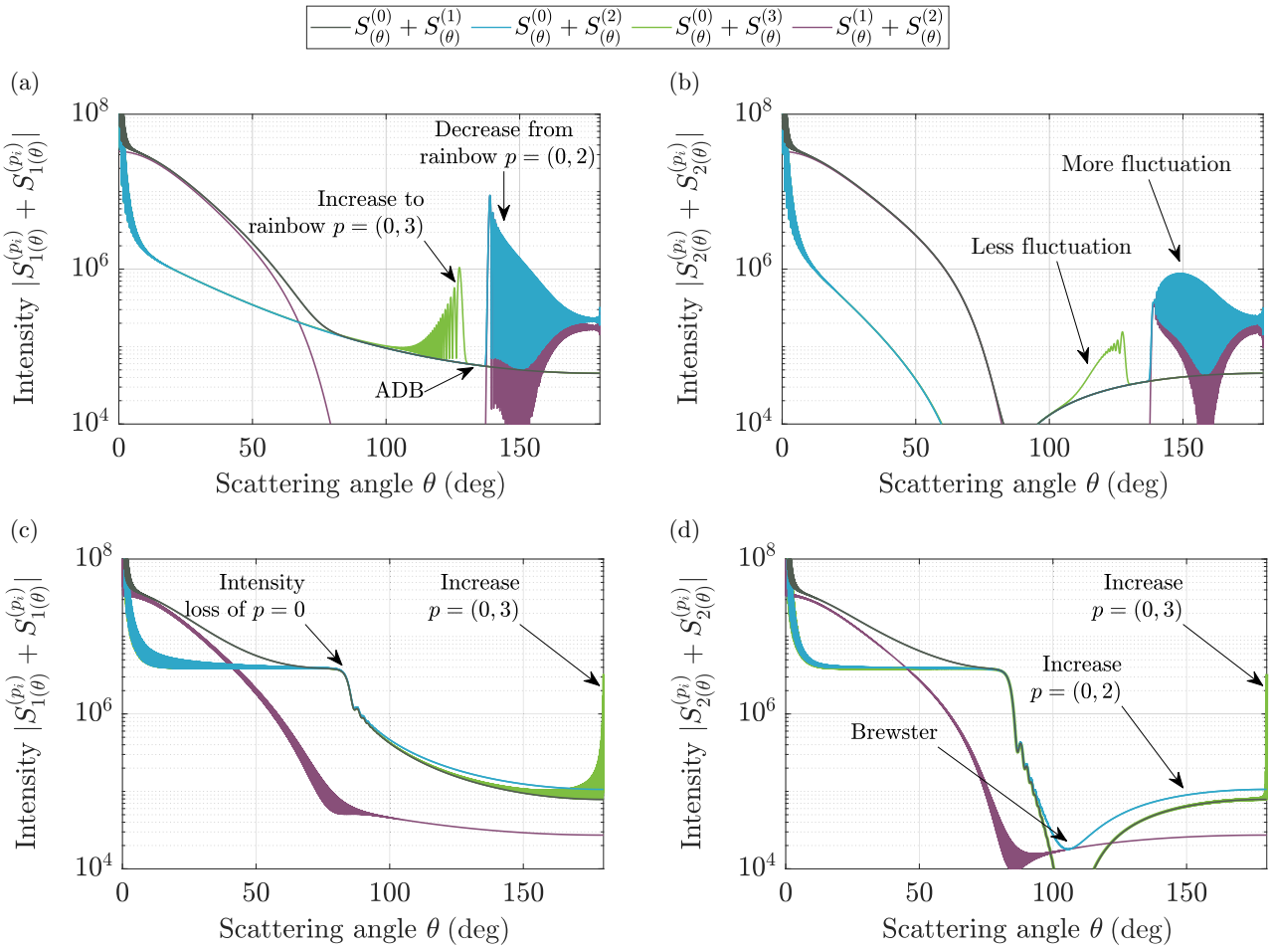

FIG. 13. Debye plots of the peak intensity of the interference pattern for (a,b) a water droplet in air ($m = 1.333 + i1.82\times10^{-9}$, $\lambda = 532\ \mu\text{m}$, $d_p = 250\ \mu\text{m} \Rightarrow x = 1476.3$) in (a) TE mode and (b) TM mode, and for (c,d) an air bubble in water ($m = 1/1.333 + i0$, $\lambda = 532\ \mu\text{m}$, $d_p = 250\ \mu\text{m} \Rightarrow x = 1967.9$) in (c) TE mode and (d) TM mode.

Finally, the intensity of the glare points depends on the scattering angle, so the SNR is also a function of θ. The relationship between scattering angle and intensity is highly nonlinear. To assess the SNR of the interference pattern, the intensities of its maxima can be examined. These can be calculated from the combined intensity of the two glare points forming the pattern, $I_{\mathrm{PI,max}} = |S^{(p_i)} + S^{(p_j)}|$ (see Fig. 13). This quantity provides a brightness measure for the maxima of the interference patterns (i.e., its distinction from the background—the SNR), while the intensity difference between the minima and maxima of the pattern is evaluated on the grounds of the visibility. Consequently, both should be taken into account, as both influence the signal quality.

For droplets in TE and TM mode, a strong decrease of intensity from the front- to the side-scatter can be seen [compare Figs. 13(a) and 13(b)]. From the side-scatter regime toward the $p = (0, 3)$ rainbow angle, the intensity increases with the scattering angle, while from the $p = (0, 2)$ rainbow angle, the intensity decreases toward even larger scattering angles. As observed for the visibility, the intensity is also low in the ADB, making this angle range unfavorable for IPI. In general, the backscatter regime for droplets shows higher intensities, making it more favorable than the side-scatter regime. However, large fluctuations in intensity [see, e.g., Fig. 13(b)] cause large variations in SNR for even small changes in angle, as might occur for particles moving through the field of view.

For bubbles also a strong decline of intensity is observed when moving beyond the front-scatter regime [compare Figs. 13(c) and 13(d)]. For bubbles in TE mode the intensity—and therefore the SNR—decreases with increasing scattering angles, which makes experimentation with these angle ranges difficult. Notably, there is a strong increase of intensity for scattering angles close to 180°, while the visibility in this region is also sufficient. For the TM mode, the intensity decreases toward the Brewster angle, but increases afterwards again [see Fig. 13(d)]. This is valuable information, as it indicates an increasing SNR in backscatter with increasing scattering angles. This means that larger scattering angles are potentially favorable for backscatter in TM mode.

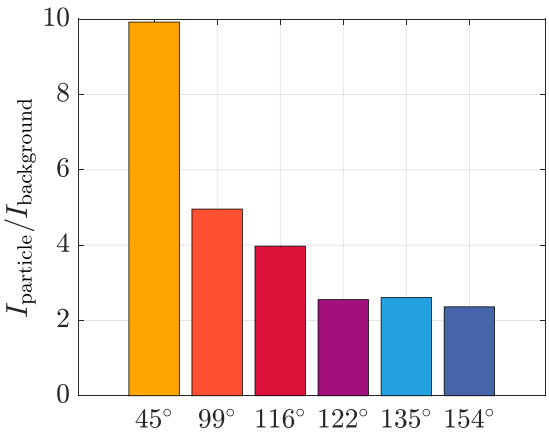

FIG. 14. The signal strength (mean intensity of the maxima in every PI) over the background intensity for the images used in the validation experiment. The values correspond to the images shown in Fig. 11(a). It can be seen that the particles gradually become less distinct from the background and the intensity decreases from the front- over the side- into the backscatter region.

The comparison of Figs. 13(c) and 13(d) furthermore reveals that the TE mode has in general higher intensities in the side- and backscatter regimes. Similar to the TE mode, the TM mode shows a sudden increase in intensity for scattering angles close to 180°. However, this higher intensity is within a very narrow angular range, which again causes problems for particles moving through the field of view. Scattering angles approaching 180° present an additional challenge, as coherent backscatter (CBS) [35] in this range can distort the fringe pattern and must be taken into account. However, since such extreme angles are primarily relevant to microscopic imaging but not for the present setup, they are not considered further in this study.

Comparison of Figs. 5 and 13, in contrast, outlines the complex relationship between visibility and SNR, but also indicates both tradeoff and synergetic angle margins, with synergistic angles being preferred.

To test the theoretical approach to SNR issues based on the intensities calculated from the LMT, the PIs from the validation experiment were investigated for their SNR (see Fig. 11). While it is difficult to determine the exact SNR, the overall ratio of PI intensity to background intensity, $I_{\mathrm{PI}}/I_{\mathrm{BG}}$, can be used as a measure of SNR. The PI intensity is defined here as the average value of the 50 brightest pixels within the bounding box that encloses the PI. The background intensity is defined as the average intensity of a 200×200 px^2 patch in the image that does not contain a PI.

A set of example images as used to compute the SNR is shown in Fig. 11(a). It is important to note in this context that the brightness of the light source was increased during the validation experiments in backscatter orientation to combat lower overall intensities. Since this in turn likewise increased the background intensity, the above-defined SNR estimation provides reasonable information on the relative PI brightness despite varying absolute intensity, as shown in Fig. 14. Nevertheless, the experimental data of Fig. 14 show a good agreement with the theoretical considerations of Fig. 13(c), where the intensity decreases strongly from scattering angles of 45° compared to angles in the range of 99°–122°. The decrease from 122° to 154° is then much smaller compared to the decrease from the front- to the side-scatter regime.

The same trend can be seen in the SNR of the experimental data as indicated in Fig. 14. This suggests that the

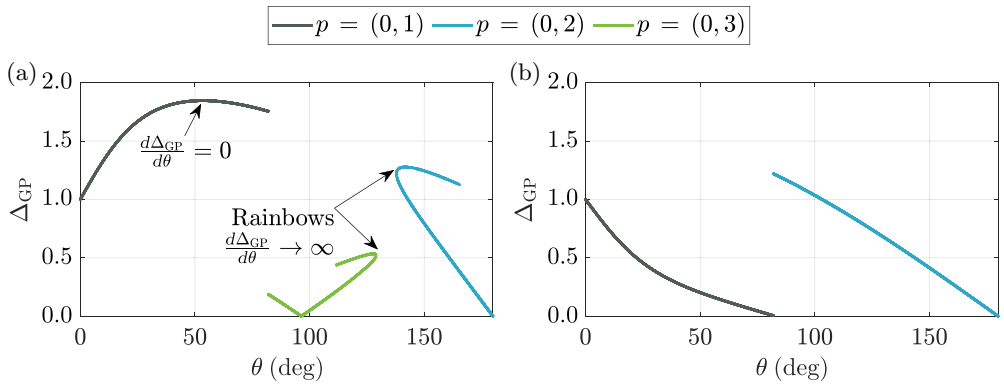

FIG. 15. Glare-point spacing $\Delta_{GP(\theta)}$ over the scattering angle for (a) droplets ($m = 1.333$) and (b) bubbles ($m = 1/1.333$). The lines are color-coded to indicate the glare-point spacing. Only the glare-point spacing of the glare-point pairing dominant at the scattering angle is shown.

combined intensity of two glare points provides a good qualitative guide to the SNR as a function of the scattering angle. However, it becomes clear from both theoretical considerations and experimental data that backscatter IPI requires methods to deal with the significantly lower SNR, such as more robust fringe frequency extraction algorithms. The lower intensities in turn also require better detection algorithms, as smaller particles generate dimmer PIs, which can fall below a given detection threshold upon data processing and accordingly bias any subsequent evaluations of particle-size distributions. In this context, machine-learning-based approaches for flow evaluation and particularly for particle detection have considerably matured in recent years [36,37] and seem promising for this unavoidable image-processing challenge.

Finally, the glare-point spacing also plays an important role in Eq. (20), as it is the only denominator and depends on the scattering angle. As described earlier, a change in the scattering angle also introduces a change in the fringe frequency for the same particle size, which must be taken into account. Note, however, that the actual influence on the fringe-pattern changes also depends on the scattering angle itself. The glare-point spacing can be obtained from Fig. 8, which is plotted over the scattering angle in Fig. 15 to emphasize this interplay.

There are two factors to consider with respect to the scattering angle—the spacing Δ_{GP} itself and its gradient $\mathrm{d}\Delta_{GP}/\mathrm{d}\theta$ upon changes of the scattering angle θ. The former directly scales with the frequency and shifts the uncertainty as well as the lower and upper limits of IPI, as shown in Fig. 12(c). The latter describes the sensitivity of the glare-point spacing to angular changes, which is described by $S_e = |\mathrm{d}\Delta_{GP}/\mathrm{d}\theta|$. This sensitivity is an important quantity for typical IPI measurements in a field of view (FOV), because particles likely move through the FOV and accordingly experience different scattering angles in consecutive frames. This means that the glare-point spacing changes—independently from any physical particle-diameter changes—and so also does the uncertainty. It appears, therefore, also beneficial to furthermore quantify the influence of this change in scattering angle for the given experimental setup in order to evaluate the influence of the range of covered scattering angles within the FOV under investigation.

For droplets, Fig. 15(a) reveals two important phenomena in the diagrams: around $\theta = 55°$ there is a plateau where the sensitivity S_e is zero, which indicates that the influence of the scattering angle on the glare-point spacing essentially vanishes. The opposite can be observed for the rainbow angles, where the gradient of S_e approaches infinity. In these two small indicated angular ranges, the sensitivity becomes large and even small location changes inside the FOV or likewise small uncertainties in the experimental setup of the angle will inevitably cause large differences in the frequency of the PI for the same particle diameter (i.e., large uncertainties). This illustrates why rainbow angles, despite their favorable high intensity, are not well suited to IPI. In the range of the intra-order split-ups of $p = 2$ and $p = 3$, where three glare points contribute to the interference pattern, several different gradients and therefore different uncertainties have to be considered at the same time. This shows that a three-glare-point IPI as proposed by Dehaeck and van Beeck [16] provides greater reliability due to redundancy, but also requires a more considered estimation of uncertainty.

The glare-point spacing for bubbles is shown in Fig. 15(b). Unlike the distinct droplet characteristics, in the case of bubbles a similar trend in the Δ_{GP} slope can be identified for both the front- and the backscatter regimes. Particularly, for the backscatter region at $\theta > 90°$, the diagram has a near-constant slope, which indicates a constant sensitivity S_e. This information is encouraging news for any IPI application in backscatter, as it demonstrates that the overall low SNR for such applications does not encounter additional uncertainty estimation issues from angle sensitivities within a chosen FOV.

VI. CONCLUDING REMARKS

In the course of this work, it has been shown that IPI can be performed in the backscatter regime. In contrast to the front-scatter regime, interference patterns in the side- and backscatter regimes are formed by different scattering orders and glare-point spacings, which requires a different transfer function between fringe frequency and particle diameter to account for these changes.

The visibility plots presented in this work can be used to identify suitable scattering angles for IPI as well as to identify the scattering orders that form the interference pattern. The visibility plots have been shown to predict the visibility of patterns from experimental images appropriately. With the GP pairing identified, GP maps and GP plots can be used to determine the respective GP spacing, as required for the transfer function between fringe pattern and particle diameter. GP maps have the advantage of giving an overview of the GP spacing at any scattering angle, while GP plots give more insight into the intensity distribution of the GP and can uncover shortcomings of the visibility approach, e.g., caused by intra-order split-ups.

The study of visibility, intensity, and GP spacing provides several insights that should be considered when selecting a scattering angle. Generally, a high SNR is desirable for a good measurement. For IPI, the SNR depends on both the visibility of the pattern (i.e., the ability to distinguish between minima and maxima in the pattern) and the intensity of the scattered light (i.e., the ability to distinguish the PI from the background). Both factors must be considered together to achieve sufficient SNR, especially in the backscatter regime. In particular, large variations in visibility or intensity can cause difficulties, since measurements with large FOVs include a range of effective scattering angles, which in turn might lead to unfavorable angles for the PIs in certain regions of the recorded image. Consequently, the measurement uncertainty can change with the in-plane position of the particle for scattering angles with strong fluctuations. To manage such intensity fluctuations, a reliable background subtraction, achieved, for example, through recorded background images or adaptive filtering, becomes crucial for evaluating PIs despite changing SNR. Furthermore, the sensitive change of the GP position for even small angle changes (especially in backscatter) moreover means that the transfer function between frequency and particle diameter effectively becomes a function of the in-plane position of the particle as well.

For droplets, the TE mode is best suited for measurements in the front-scatter region, but for the side- and backscatter region the polarization should be changed to TM mode to avoid strong intensity fluctuations and obtain more equal GP intensities. While droplets have the advantage of high intensities in the backscatter regimes compared to bubbles, measurements with droplets in side- and backscatter present several other challenges. The ADB introduces a range of scattering angles at which IPI cannot be performed due to the lack of visible GPs. Furthermore, outside of ADB, the GPs of $p = 2$ and $p = 3$ face an intra-order split, which can be useful for redundancy due to the presence of three frequencies in the interference pattern. However, this effect also requires consideration of three different uncertainties and sensitivities to angle changes, thus rendering uncertainty quantification cumbersome. At the rainbow angles, the intra-order split can be avoided, but the sensitivity of the GP spacing becomes large and, moreover, small changes in the in-plane position of the particle might lead to drastic changes in the interference pattern for the same particle size. Therefore, the transfer function becomes highly dependent on the in-plane position of the particle, adding another challenge to the measurement.

Bubbles behave significantly differently in the side- and backscatter regimes. For bubbles, both TE and TM modes are usable in the side and backscatter regimes, with the former giving higher intensities and the latter resulting in better visibility. Interestingly, a region in the side-scatter cannot be used for IPI due to the effect of the Brewster angle. Moreover, the fluctuations in intensity and visibility are much smaller for bubbles than for droplets, which renders experimentation with larger FOVs possible without the aforementioned additional uncertainty introduced by the in-plane position. Also, the angle sensitivity of the transfer function is comparable between front- and backscatter. For large scattering angles close to 180°, bubbles allow measurements with high visibility and intensity, but coherent backscatter can disturb the interference pattern.

Three main sources of uncertainty have been identified in the application of IPI. The out-of-plane position of the particle affects the defocusing parameter. This relationship is typically linear, so that uncertainties in the out-of-plane position linearly affect the size measurement. For quasi-two-dimensional measurements with known out-of-plane positions of the particles, this error is usually negligible. The second source of uncertainty comes from the GP spacing, which defines the transfer function between the interference pattern and the particle size. The spacing changes the corresponding frequency of the pattern for a given particle size. Consequently, the lower and upper limits of measurable particle sizes can be manipulated with the scattering angle. Since this also affects the resolution per stripe, the accuracy of the frequency determination can also be manipulated by changing the scattering angle.

Finally, the GP spacing affects the aforementioned sensitivity of the transfer function to angular changes, i.e., the in-plane position of the particle. The last influencing factor is the uncertainty of the frequency determination itself, which is mainly determined by the resolution of the fringes and their SNR. The SNR is influenced by the particle size (larger particles have a higher scattering efficiency) and the amount of defocusing (intensity loss due to defocusing), in addition to the visibility and intensity dictated by the

scattering angle. The resolution of the PI is determined by the amount of defocusing and the GP spacing, and thus by the particle size and scattering angle. These interrelationships lead to the following two main trade-offs. (i) For a given particle size, the scattering angle changes the fringe frequency, which, *vice versa*, can be used to calibrate the desired number of fringes for the investigated particle size distributions far away from the Nyquist criterion. This adjustment inevitably also affects both the visibility and intensity, and therefore the SNR of the PI will also change. As such, a trade-off is found between a good fringe detection accuracy and a good SNR. (ii) More defocused PIs have better spatial resolution of the PI, but at the cost of lower SNR due to intensity loss. Therefore, there is both an optimal particle size and an optimal amount of defocus to minimize the uncertainty in the frequency determination, both of which immediately rely on the given experimental situation and corresponding equipment.

Despite the lower signal quality and more complex handling of uncertainty, the backscatter regime remains of interest for IPI due to the ability to measure with a single optical access. The use of a single optical access makes IPI much more flexible and opens up the possibility of measurements closer to the actual application rather than laboratory models. In this context, the present work contributes toward a more straightforward and robust applicability of IPI for applications with limited optical access. Complementary to the presented approach, the development of advanced data evaluation methods that are more robust to low SNR appears promising for achieving further progress in IPI as a single-optical-access application. Here, the primary objectives might be the detection of particles that are less distinguishable from the background, and more robust and accurate algorithms for fringe frequency extraction.

ACKNOWLEDGMENTS

This work was funded by the Deutsche Forschungsgemeinschaft (DFG, German Research Foundation) via Project Grant KR4775/4-1 within the Research Unit FOR 5595 Archimedes (Oil-refrigerant multiphase flows in gaps with moving boundaries—Novel microscopic and macroscopic approaches for experiment, modeling, and simulation)—Project No. 510921053.

The author contributions to this work are as follows: C.S., conceptualization, methodology, investigation, software, visualization, data curation, formal analysis, validation, and writing (original draft preparation, review, and editing); M.D., methodology, formal analysis, validation, and writing (review and editing); and J.K., conceptualization, formal analysis, validation, writing (review and editing), funding acquisition, supervision, and project administration.

DATA AVAILABILITY

The data that support the findings of this article are openly available at KITopen [38].

APPENDIX A: FURTHER INFORMATION ON THE OPTICAL SYSTEM

Equation (8) requires a description of the optical system (B_{tot}, defocusing component) to calculate the particle diameter. This appendix provides more details on the computation of the value of B_{tot} in the validation experiment. Three different kinds of matrices were used. The first one is a matrix for propagation through free space of length d_i:

$$M_i = \begin{bmatrix} 1 & d_i \\ 0 & 1 \end{bmatrix}. \tag{A1}$$

The next matrix describes the refraction at an interface like a glass wall. The initial refractive index is n_1 and the index after the interface is n_2. For a curved wall the radius $R > 0$ is used to describe the curvature. For a flat interface $R \rightarrow$

ALGORITHM 1. Calculation of a line with scattering order p in a GP map.

Input: $p = p_i$ # defines the scattering order
$q = [-1, 1]$
$k = [0, 1, .., k_N]$ # k_N is the number of tries for k
$\beta_{\text{i}} = \text{linspace}(0...\pi/2, N_{\text{setps}})$ # N_{setps} defines the resolution of the GP-map
for n *in* q **do**
  for m *in* k **do**
    $\theta(:, n, m) = q(n)/2 \cdot (\beta_{\text{i}}(:) - p \cdot \arccos(1/m \cos(\beta_{\text{i}}(:)) - \pi k(m))$
$[n_\beta(:), n_q, m_k] = \text{find}(\Re\{\theta(:, n, m)\} \geq 0 \;\&\; \Re\{\theta(:, n, m)\} \leq \pi \;\&\; \Im\{\theta(:, n, m)\} = 0)$ # get entries in β_{i}, k and q arrays
$q_{\text{output}} = q(n_q)$ # get correct q
$k_{\text{output}} = k(m_k)$ # get correct k
$\theta_{\text{output}}(:) = \theta(n_\beta(:), n_q, m_k)$ # get scattering angles that match w_p
$w_p(:) = q(n_q) \cdot \cos(\beta_{\text{i}}(n_\beta(:)))$ # get glare point positions
return $q_{\text{output}}, k_{\text{output}}, \theta_{\text{output}}, w_p$

∞ is used. The matrix is as follows:

$$M_{\mathrm{I}_{12}} = \begin{bmatrix} 1 & 0 \\ (n_1 - n_2)/(Rn_2) & n_1/n_2 \end{bmatrix}. \quad \text{(A2)}$$

The third required matrix describes a thin lens with focal length f_{lens}:

$$M_{\mathrm{lens}} = \begin{bmatrix} 1 & 0 \\ -1/f_{\mathrm{lens}} & 1 \end{bmatrix}. \quad \text{(A3)}$$

The optical system comprises propagation through free space from the bubble to the glass wall (M_{water}), the interface between water and glass ($M_{\mathrm{I_{wg}}}$), propagation through the glass (M_{glass}), the interface between glass and air ($M_{\mathrm{I_{ga}}}$), propagation from the glass wall to the imaging lens (M_{air}), the change in the light path at the imaging lens (M_{lens}), and finally propagation from the lens onto the camera chip (M_{image}) [see Fig. 10(c)]. The total system is then computed from

$$M_{\mathrm{tot}} = M_{\mathrm{image}} M_{\mathrm{lens}} M_{\mathrm{air}} M_{\mathrm{I_{ga}}} M_{\mathrm{glass}} M_{\mathrm{I_{wg}}} M_{\mathrm{water}}. \quad \text{(A4)}$$

APPENDIX B: ALGORITHM FOR THE CALCULATION OF GLARE-POINT MAPS

The calculation of GP maps as conducted alongside Eq. (16) is based on

$$\theta' = 2(\beta_i^{(p)} - p\beta_t^{(p)}) = 2\pi k + q\theta \quad \text{(B1)}$$

and Snell's law. As mentioned before, q is ± 1 and $k \in \mathbb{N}$ is an integer. The values of q and k remain to be determined, where only one combination of q and k satisfies the equation for a given refractive index m and scattering order p. A method to determine q and k while computing $w_{(\theta)}$ is demonstrated in Algorithm 1, which is based on a selective trial-and-error approach.

Algorithm 1 works as follows. For a given scattering order p and refractive index m, Eq. (16) is solved indirectly, by inserting values of $\beta_i^{(p)} = [0, \pi/2]$ into the equation and calculating the resulting values of θ. This is done for every value of $q = \{-1, 1\}$, and $k = [0, 1, 2, \ldots, k_N]$ (for low scattering orders, $k_N = 5$ is sufficient) in a trial-and-error approach. This results in $N_{\mathrm{tries}} = 2k_N$ different arrays for $\theta(\beta_i^{(p)})$. The correct values of q and k can be determined by constraints on θ. The constraints for correct solutions of the equation are $\Re\{\theta\} \in [0, \pi]$ and $\Im\{\theta\} = 0$, which is satisfied only for one pair of values of q and k.

Also, not all values of $\beta_i^{(p)} = [0, \pi/2]$ result in $\Re\{\theta\} \in [0, \pi]$ and $\Im\{\theta\} = 0$, since the required conditions for a $\beta_i^{(p)}$ determination are not given for the full range $[0, \pi/2]$. The correct entries of the $\beta_i^{(p)}$ array can be identified by the entries that satisfy the constraints on θ. The truncated arrays θ_{output} and β_{output} are defined as the set of values in θ and β that satisfy the constraints on θ. The glare-point position w of order p is then computed by inserting the values of β_{output} and q into Eq. (1).

Algorithm 1 returns the two arrays of θ_{output} and w_p, and the used values of q and k. The values of q and k for $m > 1$ and $m < 1$ are given for the first four scattering orders $p = [0, 3]$ in Table II.

TABLE 2. The k and q values for the calculation of $\beta_i^{(p)}$ and $\beta_t^{(p)}$ in Eq. (16).

p	k for $(m > 1)$	q for $(m > 1)$	k for $(m < 1)$	q for $(m < 1)$
0	0	1	0	1
1	0	−1	0	1
2	0	−1	0	−1
3	−1	1	1	1

[1] L. Kirsten, T. Domaschke, C. Schneider, J. Walther, S. Meissner, R. Hampel, and E. Koch, Visualization of dynamic boiling processes using high-speed optical coherence tomography, Exp. Fluids **56**, 52 (2015).

[2] B. Behroozpour, P. A. M. Sandborn, M. C. Wu, and B. E. Boser, Lidar system architectures and circuits, IEEE Commun. Mag. **55**, 135 (2017).

[3] M. Maeda, Y. Akasaka, and T. Kawaguchi, Improvements of the interferometric technique for simultaneous measurement of droplet size and velocity vector field and its application to a transient spray, Exp. Fluids **33**, 125 (2002).

[4] Y. Hardalupas, S. Sahu, A. Taylor, and K. Zarogoulidis, Simultaneous planar measurement of droplet velocity and size with gas phase velocities in a spray by combined ILIDS and PIV techniques, Exp. Fluids **49**, 417 (2010).

[5] K. Matsuura, K. Zarogoulidis, Y. Hardalupas, A. Taylor, T. Kawaguchi, D. Sugimoto, and K. Hishida, Simultaneous planar measurement of size and three-component velocity of droplets in an aero-engine airblast fuel spray by stereoscopic interferometric laser imaging technique, in *10th International Conference on Liquid Atomization and Spray Systems, ICLASS 2006* (2006).

[6] N. Fujisawa, A. Hosokawa, and S. Tomimatsu, Simultaneous measurement of droplet size and velocity field by an interferometric imaging technique in spray combustion, Meas. Sci. Technol. **14**, 1341 (2003).

[7] C. Dunker, C. Roloff, and A. Grassmann, Interferometric laser imaging for in-flight cloud droplet sizing, Meas. Sci. Technol. **27**, 124004 (2016).

[8] J. J. Kielar, Y. Wu, S. Coëtmellec, D. Lebrun, G. Gréhan, and M. Brunel, Size determination of mixed liquid and frozen water droplets using interferometric out-of-focus imaging, J. Quant. Spectrosc. Radiat. Transfer **178**, 108 (2016).

[9] A. Quérel, P. Lemaitre, M. Brunel, E. Porcheron, and G. Gréhan, Real-time global interferometric laser imaging for

the droplet sizing (ILIDS) algorithm for airborne research, Meas. Sci. Technol. **21**, 015306 (2009).
[10] G. Lacagnina, S. Grizzi, M. Falchi, F. D. Felice, and G. P. Romano, Simultaneous size and velocity measurements of cavitating microbubbles using interferometric laser imaging, Exp. Fluids **50**, 1153 (2011).
[11] T. Kawaguchi, Y. Akasaka, and M. Maeda, Size measurements of droplets and bubbles by advanced interferometric laser imaging technique, Meas. Sci. Technol. **13**, 308 (2002).
[12] Y. Niwa, Y. Kamiya, T. Kawaguchi, and M. Maeda, Bubble sizing by interferometric laser imaging, in *10th International Symposium on Application of Laser Techniques to Fluid Mechanics* (2000).
[13] G. König, K. Anders, and A. Frohn, A new light-scattering technique to measure the diameter of periodically generated moving droplets, J. Aerosol. Sci. **17**, 157 (1986).
[14] A. R. Glover, S. M. Skippon, and R. D. Boyle, Interferometric laser imaging for droplet sizing: A method for droplet-size measurement in sparse spray systems, Appl. Opt. **34**, 8409 (1995).
[15] C. Mounaïm-Rousselle and O. Pajot, Droplet sizing by Mie scattering interferometry in a spark ignition engine, Part. Part. Syst. Charact. **16**, 160 (1999).
[16] S. Dehaeck and J. van Beeck, Multifrequency interferometric particle imaging for gas bubble sizing, Exp. Fluids **45**, 823 (2008).
[17] H. Shen, S. Coëtmellec, G. Grehan, and M. Brunel, Interferometric laser imaging for droplet sizing revisited: Elaboration of transfer matrix models for the description of complete systems., Appl. Opt. **51**, 5357 (2012).
[18] H. Zhang, X. Wang, J. Sun, D. Jia, and T. Liu, Multidispersed bubble-size measurements by interferometric particle imaging at scattering angles of 90° and 45°, Appl. Opt. **57**, 10496 (2018).
[19] P. Russell, J. A. Venning, B. W. Pearce, and P. A. Brandner, Calibration of Mie scattering imaging for microbubble measurement in hydrodynamic test facilities, Exp. Fluids **61**, 93 (2020).
[20] H. C. van de Hulst and V. Twersky, *Light Scattering by Small Particles*, Dover Books on Physics (Dover Publications, 1957 // 1958).
[21] H. C. van de Hulst and R. T. Wang, Glare points, Appl. Opt. **30**, 4755 (1991).
[22] O. S. Heavens, R. W. Ditchburn, and S. George, *Insight Into Optics, Chapter 4.13* (American Journal of Physics, Chichester, 1992), 1st ed.
[23] A. Lipson, S. G. Lipson, and H. Lipson, *Optical Physics* (Cambridge University Press, New York, 2010), 4th ed.
[24] N. Roth, K. D. I. Anders, and A. Frohn, Determination of size, evaporation rate and freezing of water droplets using light scattering and radiation pressure, Part. Part. Syst. Charact. **11**, 207 (1994).
[25] N. Semidetnov and C. Tropea, Conversion relationships for multidimensional particle sizing techniques, Meas. Sci. Technol. **15**, 112 (2003).
[26] M. Born and E. Wolf, *Principles of Optics: 60th Anniversary Edition* (Cambridge University Press, Cambridge, 2019).
[27] W. Brouwer, *Matrix Methods in Optical Instrument Design*, Lecture Notes and Supplements in Physics (W. A. Benjamin, 1964). https://api.semanticscholar.org/CorpusID:106436488
[28] A. Gerrard and J. M. Burch, *Introduction to Matrix Methods in Optics* (Dover Publications, Inc., New York, 1975). https://api.semanticscholar.org/CorpusID:117068193
[29] P. Debye, Das elektromagnetische Feld um einen Zylinder und die Theorie des Regenbogens, Phys. Z. **9**, 775 (1908).
[30] P. Laven, MiePlot, http://philiplaven.com/mieplot.htm [Online; last accessed March 7, 2025].
[31] V. Khare and H. M. Nussenzveig, Theory of the rainbow, Phys. Rev. Lett. **33**, 976 (1974).
[32] T. Fuchs, R. Hain, and C. J. Kähler, In situ calibrated defocusing PTV for wall-bounded measurement volumes, Meas. Sci. Technol. **27**, 084005 (2016).
[33] M. G. Olsen and R. J. Adrian, Out-of-focus effects on particle image visibility and correlation in microscopic particle image velocimetry, Exp. Fluids **29**, S166 (2000).
[34] R. Leister, T. Fuchs, and J. Kriegseis, Defocusing PTV applied to an open wet clutch: From macro to micro, Exp. Fluids **64**, 94 (2023).
[35] R. Corey, M. Kissner, and P. Saulnier, Coherent backscattering of light, Am. J. Phys. **63**, 560 (1995).
[36] S. Discetti and Y. Liu, Machine learning for flow field measurements: A perspective, Meas. Sci. Technol. **34**, 021001 (2022).
[37] R. Barnkob, C. Cierpka, M. Chen, S. Sachs, P. Mäder, and M. Rossi, Defocus particle tracking: A comparison of methods based on model functions, cross-correlation, and neural networks, Meas. Sci. Technol. **32**, 094011 (2021).
[38] The data repository is openly available at KITopen, https://doi.org/10.35097/95zej6qvxs2w6951.